ISSN 1028-8546

Volume XXIX Number 2
Section: En July 2023

Azerbaijan Journal of Physics

Fizika

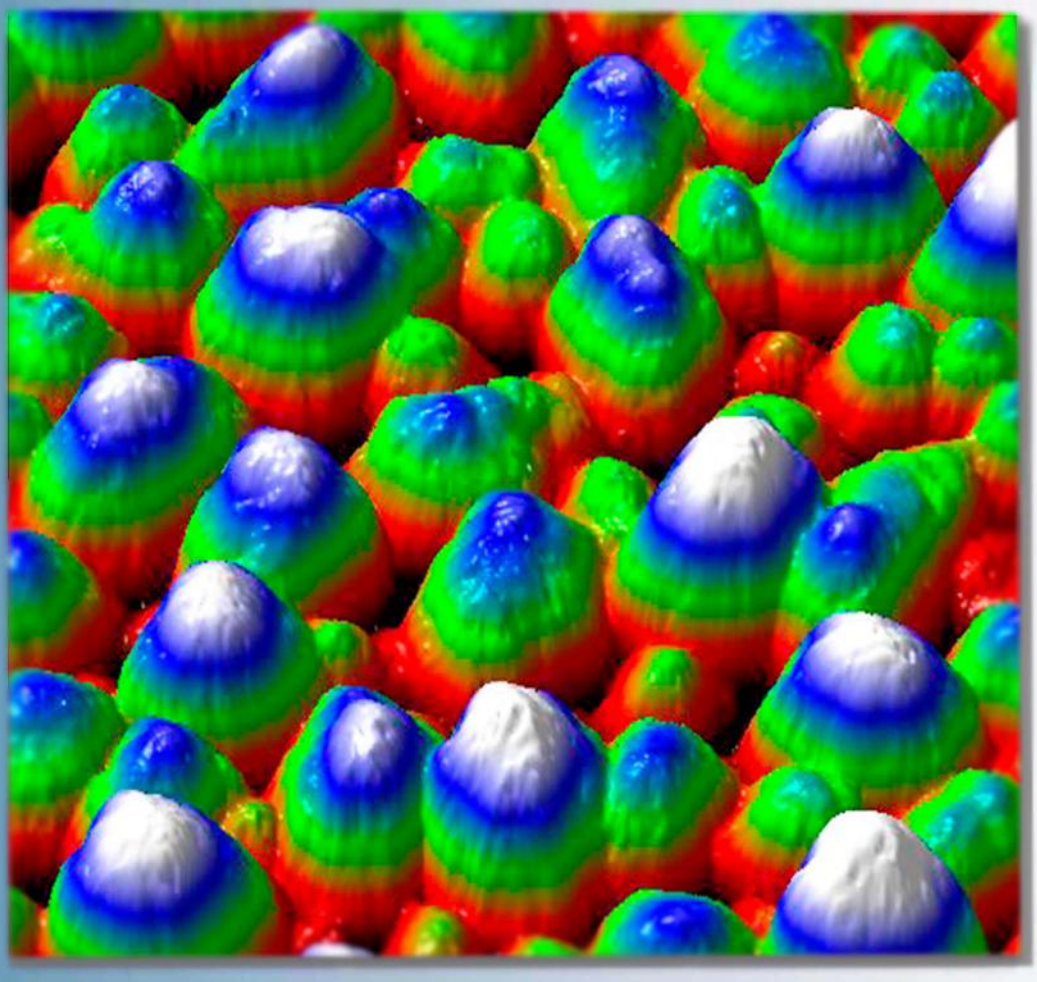

www.physics.gov.az
www.physics.gov.az/ajpfizika.html

Institute of Physics
Ministry of Science and Education Republic of Azerbaijan

Published from 1995
Ministry of Press and Information
of Azerbaijan Republic,
Registration number 514, 20.02.1995

ISSN 1028-8546
vol. XXIX, Number 02, 2023
Section: En

Azerbaijan Journal of Physics

FIZIKA

Ministry of Science and Education Republic of Azerbaijan
Institute of Physics

PUBLISHING OFFICE

131, H. Javid ave., AZ-1143, Baku
Ministry of Science and Education
Republic of Azerbaijan, Institute of Physics

Tel.: (99412) 539-51-63, 539-32-23
Fax: (99412) 537-22-92
E-mail: jophphysics@gmail.com
Internet: www.physics.gov.az

Published at "_____"
_____str., Baku

Sent for printing on: __.__. 201_
Printing approved on: __.__. 201_
Physical binding:_____
Number of copies:_____200
Order:_____

It is authorized for printing:

INVESTIGATING THE TEMPERATURE EFFECTS OF A LOW-POWER LASER ON A TISSUE-LIKE MATERIAL USING NTC-TYPE THERMISTOR SENSORS AND CALCULATING ENERGIES BY HEAT TRANSFER EQUATION

HÜSEYIN OKAN DURMUŞ[1,2,a)], BAKI KARABÖCE[2] & MIRHASAN Yu. SEYIDOV[1]

[1]Department of Physics, Gebze Technical University, 41400, Kocaeli, Turkey

[2]Medical Metrology Laboratory, TUBITAK National Metrology Institute (TUBITAK UME), 41470, Kocaeli, Turkey

E-mail: hokandurmus@gtu.edu.tr, smirhasan@gtu.edu.tr;

Tel: (262) 605 10 00; Fax: (262) 653 84 90

In this study, we aimed to investigate the temperature effects of a low-power laser on a tissue-like material, namely muscle phantom. To do this, we used thermistor temperature sensors to measure the temperature of the material at various points while it was exposed to the laser. We found that the temperature of the material increased with increasing duration of exposure to the laser, however, the maximum temperature increase was 1.7 degrees Celsius for 80 seconds, which is not harmful to tissues. Next, we applied this temperature difference information to the heat transfer equation, a mathematical model that describes how heat is transferred from one body to another. By using the measured temperature difference values and known variable such as the material's specific heat capacity, we were able to calculate the amount of energy per 1 gram produced by laser light at different distances and durations. We found that the maximum energy produced was 8.4 J for 80 s or a fluence of 0.105 J/cm² per second. This information is important because it can help us understand how the laser's energy is absorbed by the tissue-like material and how it affects the material's properties and structure. It can also provide insight into the potential therapeutic effects of low-level laser therapy, a non-invasive treatment that uses lasers to stimulate healing and reduce pain and inflammation in the body, and for determining appropriate treatment doses for various diseases.

Keywords. Tissue-Like Material, Low Power Laser, Temperature Effects, NTC-Type Thermistor Temperature Sensor, Heat Transfer Equation, Specific Heat Capacity, Energy Calculation.

INTRODUCTION

Tissue-like materials are used in many fields such as biomedical research [1], testing medical devices and instruments [2], surgical training [3], biophysics [4], and medical imaging such as ultrasound [5,6], MRI [7], CT [8,9] and PET [10]. In the field of biomedical engineering, tissue-like materials are materials that mimic the mechanical properties of biological tissues and are used in various research projects. For example, The mechanical and morphological characteristics of human anatomical features must be accurately modeled for use in medical teaching and research. While some models use preserved human cadavers or animal tissue as biological substitutes for fresh human tissue, other models are constructed of artificial materials due to both practical considerations and ethical issues [11]. In the field of testing medical devices and instruments, tissue-like materials are used to simulate the effect of devices on human tissue. For instance, the radiation impact of a cell phone may be tested using a substance that resembles tissue. As a result, it is possible to get more precise information regarding how mobile phones affect human tissue [12]. In surgical training, tissue-like materials are used to help prospective surgeons learn surgical techniques. For example, a solid model will provide the learner with something tangible to work on rather than a 2D computer-generated representation since, according to one research, 42% of new doctors do not feel confident doing an unsupervised surgery. By assisting the student in visualizing the surgery and comprehending the anatomy of the patient's organ, the realistic model can boost their confidence [13]. In the field of biophysics, tissue-like materials are used to study the physical properties of biological tissues. For instance, it is necessary to control this dose and keep it as low as practically possible to prevent biological harm to the body. This worry is taken into account, and a radiation planning technique is implemented to bring the situation safe. Before exposing the human body to the radiation technique, radiation planning involves reviewing the actual operation with tissue-like materials to determine the safety and acceptable energy range [14]. Tissue-like materials are also used in the field of medical imaging to evaluate imaging methods. For instance, high-quality tissue-mimicking phantoms (TMPs) are essential for the preclinical testing of novel diagnostic and therapeutic modalities. TMPs should be manufactured with exact T1 and T2 relaxation periods in order to precisely simulate actual tissue in Magnetic Resonance guided Focused Ultrasound (MRgFUS) applications [15]. Phantoms are also used for many other purposes, such as calibrating the optical field, testing the accuracy of measurements, and evaluating the performance of optical systems. Phantoms can also be used to evaluate the quality and performance of radiological imaging systems [16, 17]. The phantom looks as the device displays, but has previously known features. In this way, the images of the device can be evaluated for accuracy and precision. Phantoms can also be used for calibration of optical systems. For example, a phantom can be used to test the accuracy of a laser scanning system [18].

Low-level laser therapy (LLLT) is a medical treatment that utilizes lasers with low levels of energy to stimulate tissues in the body. It is sometimes referred to as "cold laser therapy" due to the fact that the lasers

131, H.Javid ave, AZ-1143, Baku
Institute of Physics
E-mail: jophphysics@gmail.com

do not generate heat when applied to the skin. LLLT devices are often used to treat a variety of conditions, including muscle and joint pain, inflammation, and wounds. The theory behind LLLT is that the low-energy lasers stimulate the cells in the body to produce energy, which can reduce pain and inflammation and promote healing. There are several factors that can impact the effectiveness of LLLT, such as the wavelength of the laser, the power of the laser, the exposure time, the intensity of the laser, the output mode, the depth of penetration, the area being treated, and the settings on the control panel. While some research supports the use of LLLT for certain conditions, further studies are needed to fully understand its effectiveness and the optimal treatment protocols. It is important to note that LLLT should not be used as a replacement for proven medical treatments, and it is always important to consult with a qualified healthcare professional before starting any new treatment. LLLT is used to treat a variety of ailments. For example, LLLT can help reduce pain. In particular, LLLT may be effective in chronic pain syndromes [19]. Again, LLLT is known to help accelerate wound healing [20]. Another example, LLLT can help reduce pain and speed up the healing process in tendonitis [21]. And finally, LLLT can help reduce pain and improve mobility in osteoarthritis [22]. Low-level laser therapy (LLLT) devices utilize low-energy lasers to apply laser beams to tissues. These lasers can operate at various frequencies and have different longitudinal modes (LMod) such as TEM00, TEM01, and TEM10, which refer to different wavelengths. The power of the laser beams, typically measured in milliwatts (mW), can be controlled by the LLLT device. LLLT devices can apply laser beams to tissues in a variety of ways, including at a single point or multiple points, with different exposure times for example ranging from 5 minutes to 30 minutes, and at different intensities and output modes, such as continuously or in waves. The depth and area of tissue that the laser beams are applied to can also vary, and LLLT devices usually have a control panel to adjust these parameters and control the device [23, 24].

Temperature measurement is an important measurement in many different fields. For example, in the health field, temperature measurement helps to measure body temperature and helps to detect whether there are health problems in cases of low or high body temperature. Normal human body temperature can vary between 36.5-37.5 degrees Celsius according to various body parts [25]. However, each individual's body temperature may differ slightly, and sometimes there may be a difference between morning and night temperature. In addition, body temperature can vary according to the age, gender and level of physical activity of the person. For example, the body temperature of children is usually slightly higher, and the body temperature of the elderly is usually slightly lower [26]. A body temperature of 37 degrees Celsius or above is defined as a high temperature or fever. In this case, it is recommended to consult a doctor.

Also, if the body temperature is 35 degrees Celsius and below, it is defined as a low temperature and it is again recommended to consult a doctor in this case.

The heat transfer equation in tissues has been investigated [27-30]. The study of heat transfer in tissues is important for various medical applications. For example, understanding the heat transfer in tissues during the design of medical devices can help evaluate the effect and safety of the device to the tissues. It can also help to understand the heat transfer in tissues of devices such as therapeutic heating and cooling pads, so that the efficacy and safety of the devices can be better understood. Treatments such as cryotherapy and radiofrequency ablation are also applied by considering the factors affecting heat transfer in tissues, and therefore understanding the heat transfer in tissues is important for the effectiveness and safety of these treatments [31,32]. Heat transfer in tissues occurs by various mechanisms, including conduction, convection, and radiation. The heat transfer equation can be used to predict the rate at which heat is transferred through tissues based on the properties of tissues (such as their thermal conductivity and specific heat capacity), the heat transfer coefficient, and the temperatures of the tissues . To accurately model heat transfer in tissues, it is important to consider the complex and inhomogeneous nature of tissues and the presence of blood vessels, which, due to their high thermal conductivity, can significantly affect heat transfer and convective heat transfer caused by blood flow. In addition to the heat transfer equation, other mathematical models and techniques, such as finite element analysis, are often used to study heat transfer in tissues and to predict the temperature distribution and thermal response of tissues to exposure to heat or cold [33]. Why is it important to investigate heat distribution in tissues? Because the distribution of tissue heat helps to understand and evaluate the heat balance in the body. The human body uses a number of mechanisms to control body temperature, and the operation of these mechanisms also affects the distribution of tissue heat. For example, when the body temperature is high, the body tries to expel the heat through water and perspiration. Therefore, the distribution of tissue heat is important for understanding the heat balance in the body. In addition, the distribution of tissue heat is also important in assessing the state of health in the body. For example, an abnormal heat distribution in an area may indicate the possibility of a health problem in that area. Therefore, investigating the distribution of tissue heat helps to understand and evaluate health status in the body [34].

In this study, we tried to understand how low-power laser exposure dissipates temperature on a tissue-like material. To do this, we used NTC-type thermistor temperature sensors to measure the temperature of the material at various points during laser exposure. This temperature difference was then applied to the heat transfer equation, a mathematical model that describes how heat is transferred from one body to another. Using the measured temperature differences and known variables such as the specific heat capacity of the material, we calculated the amount

of energy per one gram produced by the laser at different distances and times. This information can help to understand how laser energy is absorbed by the tissue-like material and affects the properties and structure of the material. It can also provide insight into the potential therapeutic effects of low-level laser therapy, a non-invasive treatment that uses lasers to promote healing and reduce pain and inflammation throughout the body.

METHODOLOGY

In this study, the muscle phantom, the VA-I-400-635 model 635 nm red-colored solid-state diode laser, UME MEDMET temperature measurement system and NTC-type thermistor temperature sensors were used. Later using the specific heat information of the muscle phantom and the detected temperature values, the energy distributions were calculated using heat transfer equations. All experiments were performed under controlled laboratory ambient conditions.

PREPARATION OF MUSCLE PHANTOM

In this study, a muscle phantom was used that was identical to one previously published by Gutierrez et al [35]. The phantom was created by mixing together agar, aluminum oxide, distilled water and heating the mixture until it reached a 80 °C temperature. After dropping the temperature of the solution to 60 °C, 10 mL of glycerin was added to the solution and then the solution was poured into a special designed measurement mold and allowed to freeze. This process was used to create a model that could be used to study the properties of muscle tissue.

LASER SOURCE

The VA-I-400-635 model of the Optotronics brand, which is a red-colored solid-state diode laser with a 635 nm wavelength, was used as the optical source for the measurements. The laser utilized in the study can be seen in Figure 1.

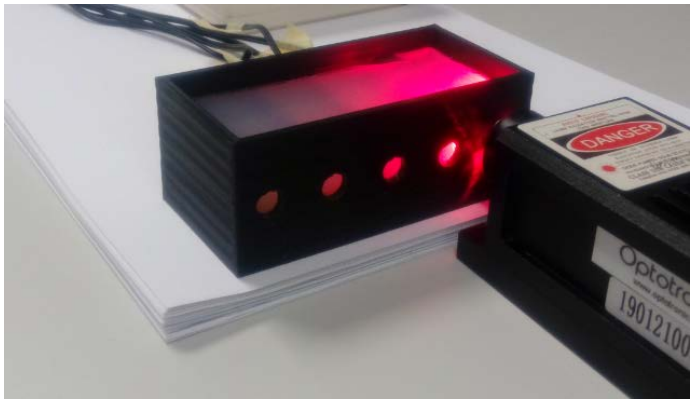

Fig. 1. A picture of the laser used in the study.

TEMPERATURE MEASUREMENT SYSTEMS AND NTC-TYPE THERMISTOR TEMPERATURE SENSORS

The temperature measurement system used in the study was the UME MEDMET system developed by our laboratory. It employed NTC-type thermistor temperature sensors and had five connectable 10 kΩ sensors with a sensitivity of 0.5%. A picture of measurement system and phantom container can be seen in Figure 2.

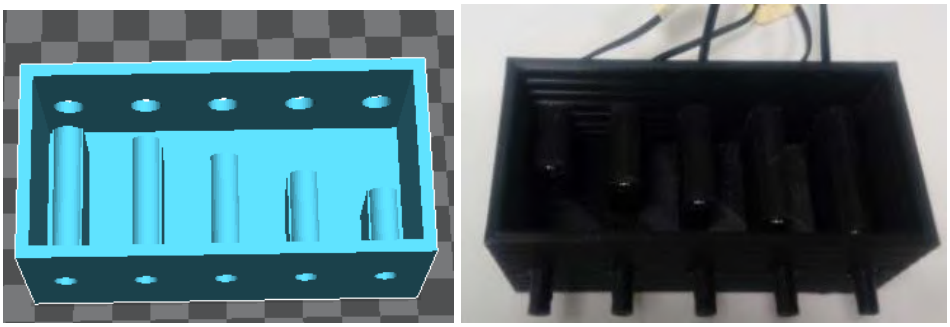

Fig. 2. Temperature Measurement Systems and NTC-Type Thermistor Temperature Sensors.

In the experiment, measurements were taken by applying the laser from various points, as shown in Figure 3. The Temperature Measurement Device (UME MEDMET) used in this experiment was developed in-house and allows for the connection of five 10 kΩ NTC type thermistor temperature sensors. The device's outer box was designed using the Solidworks program and printed on the 3D printer (Zaxe X1+) in the laboratory. It receives power directly from the connected computer through a USB connection and has a TFT touch screen for inputting commands and reading data. The device's software was also developed in the laboratory, and data can be transferred to an MS Excel file if desired.

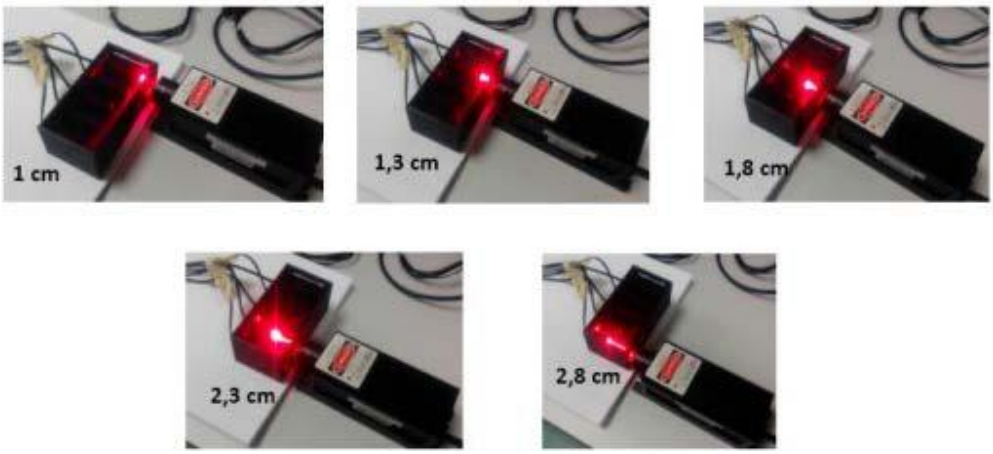

Fig. 3. The pictures of measurement points in the phantom container.

HEAT TRANSFER EQUATION AND PHANTOM'S SPECIFIC HEAT INFORMATION

The heat transfer equation is a mathematical expression that describes the rate at which heat is transferred from one place to another as a function of various physical properties and conditions. It is typically used in various engineering and scientific applications to estimate the rate of heat transfer between two bodies or between an object and its surroundings. The quantitative relationship between heat transfer and temperature change contains all three factors [36];

$$Q = mc\Delta T \quad (1)$$

where "Q" is the symbol for heat transfer, "m" is the mass of the substance, and "ΔT" is the change in temperature. The symbol c stands for specific heat and depends on the material and phase. The specific heat is the amount of heat necessary to change the temperature of 1.00 kg of mass by 1.00 °C. The specific heat is a property of the substance; its SI unit is or J/(kg·K) or J/(kg·°C). Recall that the temperature change (ΔT) is the same in units of kelvin and degree Celsius. If heat transfer is measured in kilocalories, then the unit of specific heat, kcal/(kg·°C). By using the heat transfer equation, we can predict how much heat will be transferred between two bodies or regions under given conditions, which can be useful for designing and optimizing heat transfer systems and devices, such as heat exchangers, boilers, and refrigerators. In the energy calculation of the muscle phantom, the specific heat value is taken as an average of 3650 J/(kg·°C) as literature information [37].

RESULTS AND DISCUSSION

The temperature and heat distribution graphs caused by the low-power laser applied to the muscle phantom at different times are given below. Figure 4 shows the temperature distribution created by the low-power laser in the experimental setup for 20, 40, 60 and 80 s times.

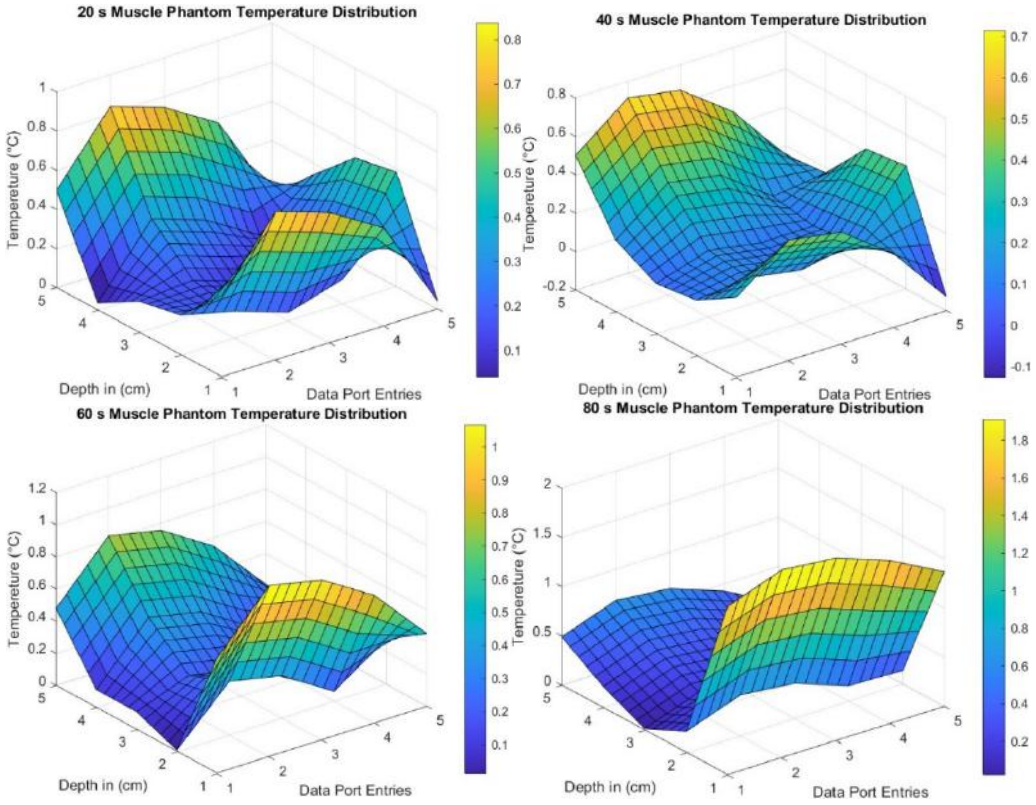

Fig. 4. The temperature distribution created by the low-power laser in the experimental setup for 20, 40, 60 and 80 s durations.

Figure 5 shows the energy distributions calculated using the measured temperature differences and the specific heat capacity of the muscle phantom for the 20, 40, 60 and 80 s times.

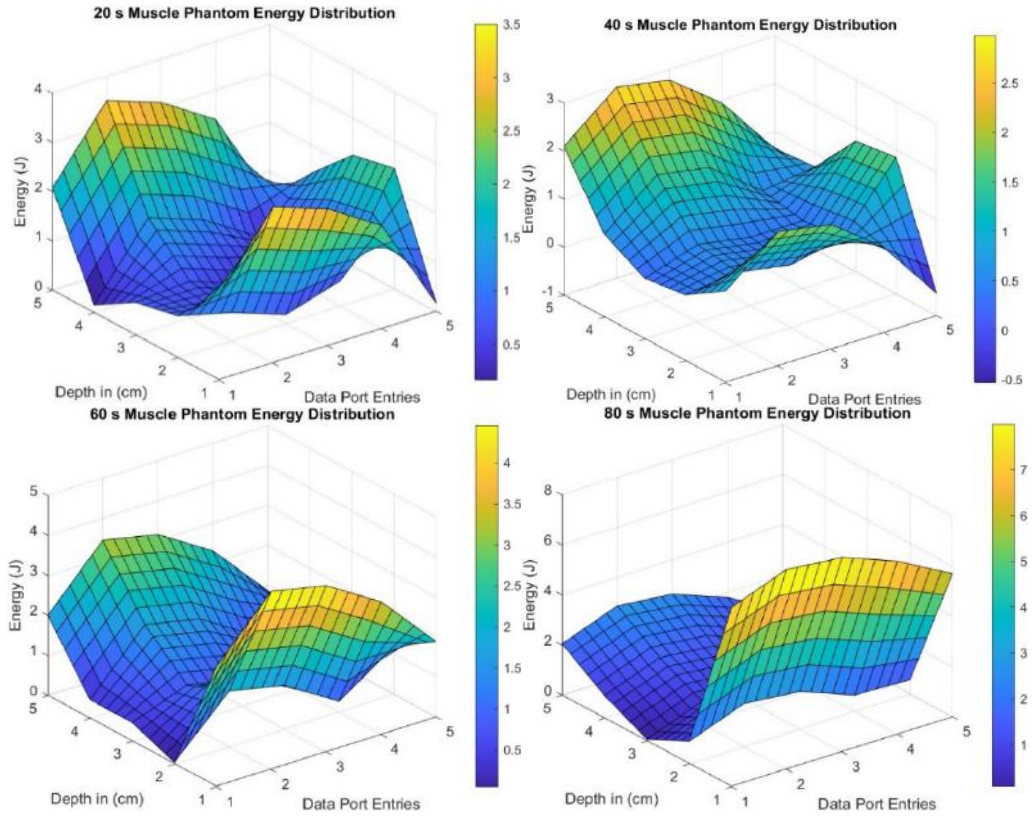

Fig. 5. The energy distribution created by the low-power laser in the experimental setup for 20, 40, 60 and 80 s durations.

DISCUSSION

In this study, laser-induced temperature measurement was investigated using NTC-type thermistor temperature sensors and UME-MEDMET temperature measurement system inside the muscle phantom. All the experiments done for temperature measurements were carried out under laboratory ambient conditions (Temperature was 23.0 °C ± 3 °C, and relative humidity was 50 rh% ± 5 rh%). It is seen that the temperature of the material increases with the increase of the exposure time of the material to the laser. The temperature rises over time can be seen much more clearly from the graphs. The temperature increases caused by the laser in the muscle phantom are a maximum of 1.7 Celsius degrees for 80 s. The maximum temperature detected was found as 23.4 °C and the average temperatures measured when the laser was applied were found as 21.7 ± 0.5 °C. When we add the maximum temperature difference and temperature uncertainty (0.94 °C) coming from the NTC type thermistor temperature sensor [38] to the average temperatures found for the muscle phantom, the temperature value to be formed will be 24.8 °C at the most. We can also adapt this assessment to human body temperature. Because the human body temperature is 37 +/- 0.5 °C [25], the maximum temperature increase found will lead to a maximum increase of 3.2 °C in body temperature, taking into account the temperature uncertainty of the measurements and the uncertainty of the NTC temperature sensor. This can raise body temperature to 40.2 ± 0.5 °C. These temperatures are harmless. Because temperatures exceeding 45 degrees cause damage to the tissues [39]. Therefore, these temperatures will only produce photochemical effects, also known as biostimulation. In other words, the laser used will not create irreversible effects. The temperatures and temperature differences found are mostly of the type that trigger photochemical processes rather than photothermal effects. At the same time, it is seen that the 400 mW laser can be used safely on people up to 80 seconds and a minimum approach distance of 25 mm.

We can also say the following about the energy distributions calculated over the detected temperatures. The heat increases caused by the laser in the muscle phantom were calculated as 8.4 J maximum for 80 seconds. In laser treatment for various diseases and symptoms, there are specific guidelines for the number of treatments, the intervals between treatments, and the method and dosage (measured in fluence, or J/cm^2) that should be followed, as outlined in a reference source [40]. The calculated energy of 8.4 J for 80 s corresponds to 0.105 J/cm^2 per second. For this reason, appropriate treatment planning can be made for the energies defined for the treatment of various diseases. For example, the following doses (fluences) per cm^2 are applied in the treatment of the following diseases and symptoms; Carpal-tunnel (8 J/cm^2), Supraspinatus (8 J/cm^2), Patellar tendon (8 J/cm^2), Achilles tendon (8 J/cm^2), Acne Vulgaris (5 J /cm^2), Allergic rhinitis (5 J/cm^2), Arthritis (5 J/cm^2), Wound healing (edge of wound) (5 J/cm^2), Scars and pregnancy stretch marks (5 J/cm^2), Muscle knots and pain (5 J/cm^2) and Tendinitis (5 J/cm^2).

CONCLUSION

In conclusion, tissue-like materials are widely used in various fields, including biomedical research, testing medical devices and instruments, surgical training, biophysics, and medical imaging. These materials are used to mimic the mechanical properties of biological tissues and are valuable for studying the physical properties of tissues, evaluating imaging methods, calibrating optical systems, and more. Low-level laser therapy (LLLT) is a medical treatment that uses low-energy lasers to stimulate tissues in the body and is used to treat a range of conditions, including muscle and joint pain, inflammation, and wounds. While there is some evidence to support the use of LLLT for certain conditions, more research is needed to fully understand its effectiveness and the optimal treatment protocols.

Based on the results of this study, it can be concluded that the use of the 400 mW laser on people for up to 80 seconds with a minimum distance of 25 mm is safe and will not produce harmful, irreversible effects. The laser caused an increase in temperature of the muscle phantom, with a maximum increase of 1.7 °C for 80 seconds. When considering the uncertainty in the temperature measurement and the sensor used, this could potentially lead to an increase of 3.2 °C in human body temperature, bringing it to a safe level of 40.2 ± 0.5 °C. The temperatures and temperature differences produced by the laser are mostly of the type that trigger photochemical processes rather than photothermal effects. As for the produced energy, the heat increase caused by a laser in a muscle phantom was calculated to be 8.4 J maximum over 80 seconds. This corresponds to a fluence (energy per unit area) of 0.105 J/cm^2 per 1 s. There are specific guidelines for the number and timing of laser treatments for various diseases and symptoms, and the appropriate treatment can be planned based on the energy levels defined for each condition. Future studies could examine the use of lasers with different powers and different types of phantoms to further understand the effects of laser-induced temperature measurement.

ACKNOWLEDGMENT

We would like to thank to Dr. Eyüp Bilgiç from Acoustics Laboratory of TUBITAK UME and our trainee, Mehmet Gökalp Köreken, from the Faculty of Biomedical Engineering in TOBB University of Economics and Technology for their contribution to our conceptional evaluation and Mathlab drawing studies.

[1] *C. K. McGarry, L.J. Grattan, , A. M. Ivory, F. Leek, G.P. Liney, Y. Liu, C.H. Clark.* 2020 Tissue mimicking materials for imaging and therapy phantoms: a review. Physics in Medicine & Biology, 65(23), 23TR01.

[2] *K. Wang, Y. Zhao, Y. H. Chang, Z. Qian, C. Zhang, B. Wang, M.J. Wang.* 2016. Controlling the mechanical behavior of dual-material 3D printed meta-materials for patient-specific tissue-mimicking phantoms. Materials & Design, 90, 704-712.

[3] *R. Murniati, E. Wibowo,M. Rokhmat, F. Iskandar, M. Abdullah.* 2017. Natural rubber nanocomposite as human-tissue-mimicking materials for replacement cadaver in medical surgical practice. Procedia engineering, 170, 101-107.

[4] *E. Bachmann, A. B. Rosskopf, T. Götschi, M. Klarhöfer, X. Deligianni, M. Hilbe, M.A. Fischer.* 2019. T1-and T2*-mapping for assessment of tendon tissue biophysical properties: a phantom MRI study. Investigative Radiology, 54(4), 212-220.

[5] *E.L. Madsen, J.A. Zagzebski, G.R. Frank.* An anthropomorphic ultrasound breast phantom containing intermediate-sized scatterers, Ultrasound Med. Biol., 8 (4) (1982), pp. 381-392.

[6] *M.K. Sun, J. Shieh, C.W. Lo, C.S. Chen, B.T. Chen, C.W. Huang, W.S. Chen.* Reusable tissue-mimicking hydrogel phantoms for focused ultrasound ablation, Ultrason. Sonochem., 23 (2015), pp. 399-405

[7] *E.L. Madsen, G.D. Fullerton.* Prospective tissue-mimicking materials for use in NMR imaging phantoms, Magn. Reson. Imaging, 1 (3) (1982), pp. 135-141

[8] *M.W. Kusk, J. Stowe, S. Hess, O. Gerke, S. Foley.* 2023. Low-cost 3D-printed anthropomorphic cardiac phantom, for computed tomography automatic left ventricle segmentation and volumetry–A pilot study. Radiography, 29(1), 131-138.

[9] *J. Greffier, Q. Durand, J. Frandon, S. Si-Mohamed, M. Loisy, , F.de Oliveira, D. Dabli.* 2023. Improved image quality and dose reduction in abdominal CT with deep-learning reconstruction algorithm: a phantom study. European Radiology, 33(1), 699-710.

[10] *S. Seeger, E. Elmoujarkach, N. Möller, C. Schmidt, M. Rafecas.* 2022. 3D printed radioactive phantoms for Positron Emission Tomography. Transactions on Additive Manufacturing Meets Medicine, 4(S1), 640-640.

[11] *S.J. Estermann, D.H. Pahr, A. Reisinger.* 2022. Material design of soft biological tissue replicas using viscoelastic micromechanical modelling. Journal of the Mechanical Behavior of Biomedical Materials, 125, 104875.

[12] *I. Develi.* Experimental Investigation of the Heating Effects of 900 Mhz Cell Phones on Brain Phantom in Terms of Public Health.

[13] *M. Higgins, S. Leung, N. Radacsi.* 2022. 3D Printing Surgical Phantoms and their Role in the Visualization of Medical Procedures. Annals of 3D Printed Medicine, 100057.

[14] *O.M. Bello, N.M. Nora, W.M.S.W. Hassana.* Characterization of the Urethane Based Tissue Equivalent Substitute for Phantom Construction: Model Molding, XCOM and MCNPX Studies.

[15] *A. Antoniou, C. Damianou.* 2022. MR relaxation properties of tissue-mimicking phantoms. Ultrasonics, 119, 106600.

[16] *R.B. Pearlin, R.S. Livingstone, A. Jasper, S.K.N. Keshava, G. Sridhar.* 2022. Evaluation of radiation dose reduction and its effect on image quality for different flat-panel detectors. Journal of Medical Physics, 47(1), 73.

[17] *J. Greffier, Q. Durand, J. Frandon, S. Si-Mohamed, M. Loisy, F. de Oliveira, D. Dabli.* 2023. Improved image quality and dose reduction in abdominal CT with deep-learning reconstruction algorithm: a phantom study. European Radiology, 33(1), 699-710.

[18] *D.M. Cash, T.K. Sinha, W.C. Chapman, H. Terawaki, M.I. Miga, Galloway Jr, R. L.* (2003, May). Incorporation of a laser range scanner into an image-guided surgical system. In Medical Imaging 2003: Visualization, Image-Guided Procedures, and Display (Vol. 5029, pp. 269-280). SPIE.

[19] *E. Momeni, F. Kazemi, P. Sanaei-Rad.* 2022. Extraoral low-level laser therapy can decrease pain but not edema and trismus after surgical extraction of impacted mandibular third molars: a randomized, placebo-controlled clinical trial. BMC Oral Health, 22(1), 1-8.

[20] *D. Hawkins, N. Houreld, H. Abrahamse.* 2005. Low level laser therapy (LLLT) as an effective therapeutic modality for delayed wound healing. Annals of the New York Academy of Sciences, 1056(1), 486-493.

[21] *F.D.R.Guerra, C.P. Vieira, M.S. Almeida, L.P. Oliveira, A.A. de Aro, E.R. Pimentel.* 2013. LLLT improves tendon healing through increase of MMP activity and collagen synthesis. Lasers in medical science, 28(5), 1281-1288.

[22] *M.R. Hamblin.* 2013. Can osteoarthritis be treated with light?. Arthritis research & therapy, 15(5), 1-2.

[23] *M.R. Hamblin, T. Agrawal, M. de Sousa.* (Eds.). 2016. Handbook of low-level laser therapy. CRC Press.

[24] *H. Chung, T. Dai, S.K. Sharma, Y.Y. Huang, J. D. Carroll, M.R. Hamblin.* 2012. The nuts and bolts of low-level laser (light) therapy. Annals of biomedical engineering, 40(2), 516-533.

[25] *I.I. Geneva, B. Cuzzo, T . Fazili, W. Javaid .* Normal Body Temperature: A Systematic Review. Open Forum Infect Dis. 2019 Apr 9;6(4):ofz032. doi: 10.1093/ofid/ofz032. PMID: 30976605; PMCID: PMC6456186.

[26] https://medlineplus.gov/ency/article/001982.htm

[27] *A.R. Khaled, K. Vafai.* 2003. The role of porous media in modeling flow and heat transfer in biological tissues. International Journal of Heat and Mass Transfer, 46(26), 4989-5003.

[28] *R.C. Eberhart, A. Shitzer.* (Eds.). 2012. Heat Transfer in Medicine and Biology: Analysis and Applications. Volume 2 (Vol. 2). Springer Science & Business Media.

[29] *M. Fu, W. Weng, W. Chen, N. Luo.* 2016. Review on modeling heat transfer and thermoregulatory responses in human body. Journal of thermal biology, 62, 189-200.

[30] *M. M. Tung, M. Trujillo, J. L. Molina, M.J. Rivera, E.J. Berjano.* (2009). Modeling the heating of biological tissue based on the hyperbolic heat transfer equation. Mathematical and Computer Modelling, 50(5-6), 665-672.

[31] *S.L. Thomsen, J.E. Coad.* (2007, February). Developing clinically successful biomedical devices by understanding the pathophysiology of the target tissue: insights from over 25 years at the microscope. In Thermal Treatment of Tissue: Energy Delivery and Assessment IV (Vol. 6440, pp. 9-23). SPIE.

[32] *N. Bhardwaj, A.D. Strickland, F. Ahmad, L. Atanesyan, K. West, D.M. Lloyd.* 2009. A comparative histological evaluation of the ablations produced by microwave, cryotherapy and radiofrequency in the liver. Pathology, 41(2), 168-172.

[33] *M.S. Ferreira, J.I. Yanagihara.* (2009). A transient three-dimensional heat transfer model of the human body. International Communications in heat and mass transfer, 36(7), 718-724.

[34] *D. Gagnon, O. Jay, G.P. Kenny.* 2013. The evaporative requirement for heat balance determines whole-body sweat rate during exercise under conditions permitting full evaporation. The Journal of physiology, 591(11), 2925-2935.

[35] *M. I. Gutierrez, S. A.Lopez-Haro, A.Vera, L. Leija.* 2016. Experimental verification of modeled thermal distribution produced by a piston source in physiotherapy ultrasound. BioMed research international, 2016.

[36] https://phys.libretexts.org/@go/page/1587

[37] *J. B. Leonard, K.R. Foster, T.W. Athley.* 1984. Thermal properties of tissue equivalent phantom materials. IEEE Transactions on Biomedical Engineering, (7), 533-536.

[38] *H.O. Durmuş, E.Ç.Arı, B. Karaböce, M.Y. Seyidov.* 2021. Investigation of temperature effects of a 635 nm low power solid-state diode laser on agar phantom using two different thermocouples. Results in Optics, 5, 100142.

[39] *B.L. Viglianti, et al.* "Thresholds for thermal damage to normal tissues: An update," International Journal of Hyperthermia, vol. 27, no. 4, pp. 320-343, 2011, doi: 10.3109/02656736.2010.534527.

[40] https://energy-laser.com/guide-lines-for-treatment-with-laser-therapy.

Received: 29.03.2023

OPTO-ACOUSTICAL CHARACTERIZATION OF PHANTOMS

HÜSEYIN OKAN DURMUŞ[1,2,a)], BAKI KARABÖCE[2], EMEL ÇETIN ARI[2] & MIRHASAN YU. SEYIDOV[1]

[1]Department of Physics, Gebze Technical University, 41400, Kocaeli, Turkey
[2]Medical Metrology Laboratory, TUBITAK National Metrology Institute (TUBITAK UME), 41470, Kocaeli, Turkey
E-mail: hokandurmus@gtu.edu.tr, smirhasan@gtu.edu.tr; Tel : (262) 605 10 00; Fax: (262) 653 84 90

To guarantee the safe and correct operation of medical ultrasonic imaging instruments, the use of phantoms is essential during testing and evaluation. Phantoms mimic the acoustic properties of living tissue, allowing for performance tests and quality control of medical ultrasonic devices. Industry standards specify that tissue-mimicking materials used in quality control of ultrasonic devices should have specific acoustic properties. Acoustical and optical properties of two distinct tissue-mimicking materials, Zerdine and Agar, were studied and characterized in this research. Acoustical properties such as density, sound velocity, and acoustic attenuation coefficient were measured using the Pulse-Echo method and transmission technique. Optical properties were studied using a single integrating sphere system and the Kubelka-Munk function approach. The results of these studies may provide a foundation for future research on the opto-acoustical characterization of various phantoms.

Keywords. Medical Ultrasonics, Phantoms, Tissue-Mimicking Materials, Zerdine, Agar, Acoustical and Optical Properties.

INTRODUCTION

Materials can be characterized and evaluated based on how they will be used, such as their optical, thermal, mechanical, acoustical, and electrical properties. One specific type of material is called a phantom, which is used as a reference point in medical testing before a procedure is done on a living patient. Phantoms have the benefit of being able to imitate the properties of living tissue and be reused multiple times. Additionally, the use of materials that mimic biological tissue is also very common in the field of biophotonics.

It is crucial to test and evaluate the devices used in ultrasonic imaging and treatment systems to ensure they work safely and correctly. To do this, special materials called phantoms are used. These phantoms are designed to mimic the acoustic properties of the tissue being studied. This allows for performance tests and quality control of medical ultrasonic devices. In order for the measurements to be accurate and reliable, the phantom should have similar acoustic properties as human tissue. Some important physical properties that are measured when characterizing these phantoms include the speed of sound, density, characteristic acoustic impedance, and attenuation coefficient. The most important aspect of developing a phantom for use in ultrasonic imaging device testing is that it meets the standards for acoustic properties as specified in the industry standards [1,2].

Phantoms are essential for testing and evaluating medical ultrasonic imaging devices. According to industry standards such as IEC TS 62791:2015 and IEC 1390, the tissue-mimicking materials used in quality control of ultrasonic devices should have specific acoustic properties, including an ultrasonic sound velocity of (1540 ± 10) m/s and an attenuation coefficient of (0.50 ± 0.04) dB/(cm·MHz) for low attenuation coefficient echo targets and (0.70 ± 0.04) dB/(cm·MHz) for "background" materials [3,4]. These standards ensure that the tests are performed correctly and give accurate results.

When testing and evaluating phantoms, different parameters are examined depending on the type of characterization being performed. Acoustical characterization looks at parameters such as sound velocity, characteristic acoustic impedance, acoustic attenuation coefficient, and acoustic backscatter coefficient. In contrast, optical characterization examines parameters like absorption coefficient, scattering coefficient, and anisotropy factor [5]. While there is a well-established system for acoustical characterization, studies in optical characterization are still relatively new and developing.

The Kubelka-Munk model is a theoretical reflection model that is commonly used in optics. This model assumes that when light passes through a homogeneous sample, some of it is scattered and absorbed in different directions, causing the light to be weakened. The Kubelka-Munk model is a two-stream approach to general radiation transfer theory and it characterizes the spread of upstream and downstream fluxes by scattering and absorption coefficients known as S and K respectively.

This model is widely used for describing the optical properties of luminescent materials. It is one of the simplest and most successful models for predicting the optical properties of particulate films under dispersed illumination from the material's effective absorption and scattering coefficients. It has a wide range of applications in different materials such as paints, pigmented plastics or polymers, decorative and protective coatings, solar-absorbing pigments and paints, human tissue, biological systems, and optical properties. The model assumes that the optical properties of a coating can be described by two constants, the absorption and scattering coefficients [6-9].

In this study, the acoustical and optical properties of two types of phantoms, Zerdine and Agar phantoms,

131, H.Javid ave, AZ-1143, Baku
Institute of Physics
E-mail: jophphysics@gmail.com

were analyzed separately. The acoustical characterization study measured the density, sound velocities, and acoustic attenuation coefficients of the phantoms. The optical characterization study used a single integrating sphere system to measure parameters such as absorbance, transmittance, and reflectance. Additionally, the refractive index and optical linear attenuation coefficient were calculated as macroscopic optical parameters. Microscopic optical properties, such as the absorption coefficient, scattering coefficient, anisotropy factor, reduced scattering coefficient, and penetration depth were determined using the Kubelka-Munk Function approach.

METHODOLOGY

In this study, Zerdine and Agar phantoms are characterized in terms of optical and acoustical methods. In optical characterization, the Pulse-Echo method and transmission technique were utilized while a single integrating sphere system and the Kubelka-Munk function approach were used in the optical characterization. All experiments were performed under controlled laboratory ambient conditions.

PREPARATION OF ZERDINE AND AGAR PHANTOMS

Tissue-Mimicking Materials (TMMs) are materials that are often used in medical research because they are able to mimic the properties of biological soft tissues. In this study, two types of TMMs were used, named Zerdine and Agar. Zerdine phantoms are commonly used as reference materials in quality control of ultrasonic imaging systems, while Agar phantoms are typically used in ultrasonic research. The Zerdine phantom was prepared in a rectangular container using a specific formulation, as specified in a patent by Zerhouni and Rachedine [10]. The Agar phantom was created by mixing 2% Agar and 0.4 M $ZnCl_2$ by weight of the starting water in a cylindrical container [11]. A picture of the Zerdine and Agar phantoms that were tested can be seen in Figure 1.

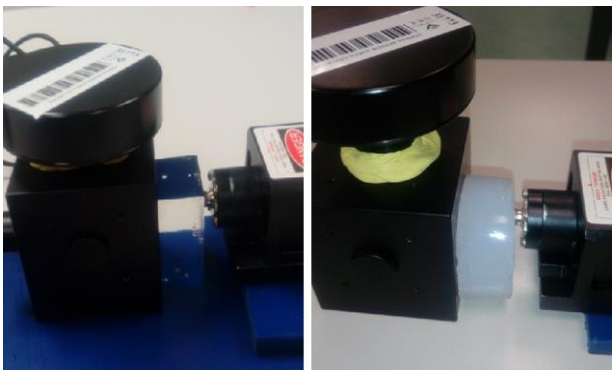

Fig. 1. A picture of the Zerdine (left) and Agar (right) phantoms under test.

SOUND VELOCITY MEASUREMENT SET-UP

The Puls-Echo method was used to measure sound velocities in this study [1,2]. The experimental setup and equipment connections used for these measurements are illustrated in Figure 2.

The Pulse-Echo method is a technique in which an ultrasonic probe, also called a transducer, is used to both transmit and receive signals. In this method, the probe is placed in contact with the phantom using an impedance matching gel and the signals sent and received by the Pulser/Receiver device are displayed on an oscilloscope screen. The period value between the observed signal peaks is recorded on the oscilloscope screen and the sound velocity is calculated using formulas (1, 2 and 3) as illustrated in Figure 4. It is important to ensure that the thickness of the sample being tested is accurately determined for the method to work correctly.

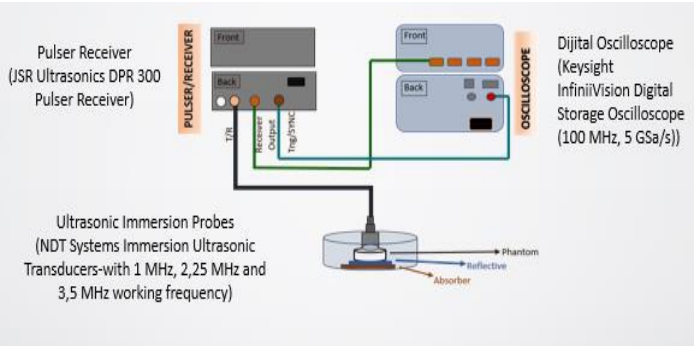

Fig. 2. Experimental setup used to determine ultrasonic sound velocity by using Pulse-Echo method.

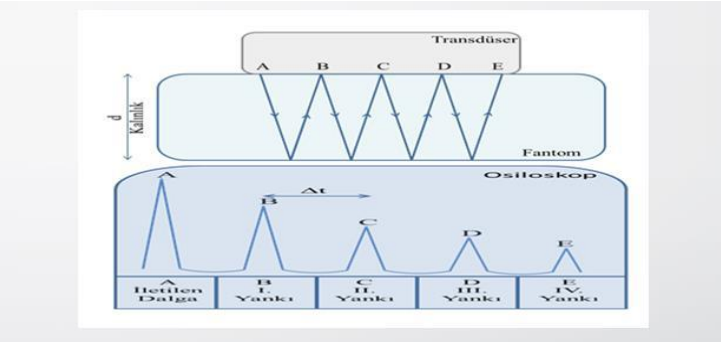

Fig. 3. Echo patterns observed in determining the speed of sound with Pulse-Echo method.

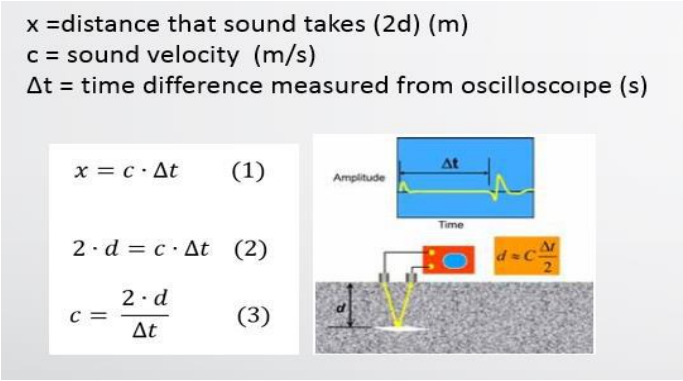

Fig. 4. Sound veocity calculation formulas.

ATTENUATION COEFFICIENT MEASUREMENTS AND SET-UP

The attenuation coefficient is determined using the "transmission" technique [1,2]. In this method, two transducers operating at the same frequency are used to generate and detect the ultrasound signal. The transducers are placed parallel to both surfaces of the sample. The amplitude of the signal that reaches the receiver transducer decreases exponentially, and the attenuation coefficient is calculated by using a specific formula.

$$A = A_0 e^{-\mu x} \quad (4)$$

The attenuation coefficient is represented by the Greek letter, μ and is measured in units of dB / cm · MHz. It is calculated using the distance (x) in centimeters, the formula is given with the Greek letter μ, and x. The experimental setup used for measuring the attenuation coefficient is illustrated in Figure 5. Every tissue has a unique attenuation coefficient, which is a representation of the decrease in ultrasonic wave amplitude after it reaches the tissue due to absorption, scattering, and conversion of mode.

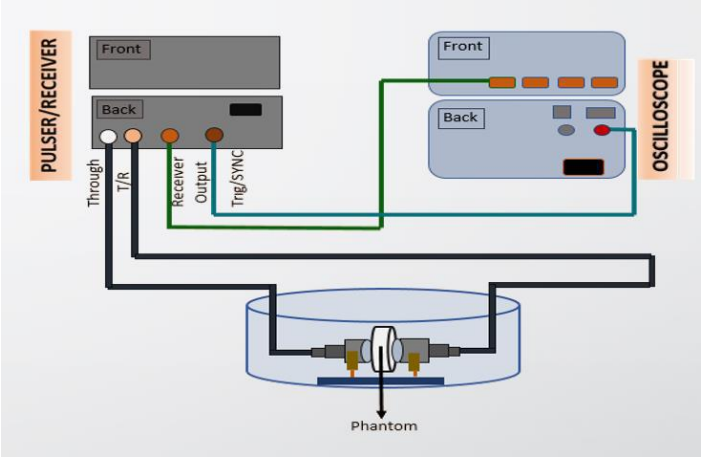

Fig. 5. Experimental setup used for attenuation coefficient measurements.

DENSITY MEASUREMENTS

Density is a measure of how much mass is contained within a certain volume of matter, and it is determined by the equation:

$$\rho = \frac{m}{V} \quad (5)$$

Where; "m" (kg) is the mass and "V" (m^3) is the volume. To determine the density of the phantom samples, the volume and mass were measured, then the density was calculated using the equation above.

ACOUSTIC IMPEDANCE CALCULATIONS

Acoustic impedance is a property of a material that describes how well it transmits sound waves and is denoted by the letter "Z" and calculated by the following equation:

$$Z=\rho \cdot c \quad (6)$$

Where; "ρ" (kg/m^3) is the density, "c" (m/s) is the sound velocity, and "Z" ($(kg/m^2) \cdot s$) is the acoustic impedance. Another unit used for acoustic impedance is Rayl.

OPTICAL MEASUREMENT EQUIPMENTS

A red colored solid-state diode laser with a wavelength of 635 nm, made by Optotronics and model VA-I-400-635, was used as the optical source for the measurements. The maximum working power of the laser was 400 mW. For the measurement of optical power, an Ophir StarBright model optical power meter and an Ophir 3A type thermal sensor were used. The Thorlabs IS200 model 2" integrating sphere was used to measure optical properties such as absorbance, transmittance, reflectance, refractive index and optical linear attenuation coefficient. All the optical measurement equipment used in the experiment are shown in Figure 6.

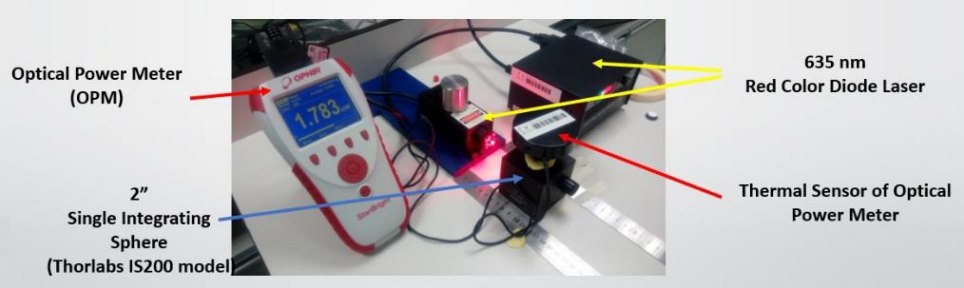

Fig. 6. Optical measurement equipment used in the experiment.

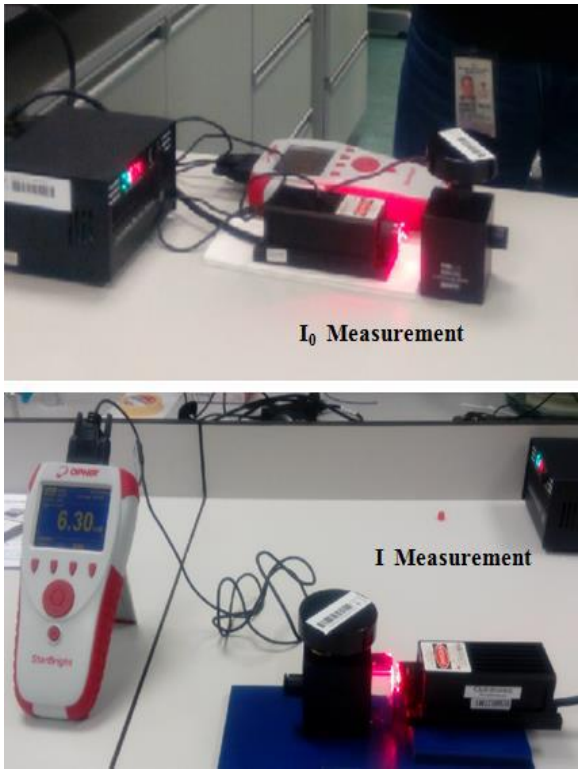

Fig. 7. Optical measurement equipment used in the experiment.

In this study, the single integrating sphere measurement method was used. Figure 7 illustrates the setup of the single integrating sphere experiment used for measuring both optical power and optical properties. The setup involves two measurements, I_o and I measurement. In the I_o measurement, there is no phantom in the system, while in the I measurement, there is a phantom in the system.

CALCULATION OF MACROSCOPIC OPTICAL PROPERTIES

The relevant formulas for macroscopic calculations of absorbance, transmittance, reflectance, refractive index, and optical linear attenuation coefficient can be seen as follows.

$$R+T+A = 1 \text{ or } \%R+\%T+\%A = \%100 \quad [12] \qquad (7)$$

Absorbance,

$$A;\ A=-\log(I/I_0)=-\log(T)=2-\log(\%T) \quad [13] \qquad (8)$$

$$\text{Transmittance, T; } T = I/I_0 \quad [13] \qquad (9)$$

$$\text{Reflectance, R; } R=1-(A+T) \quad [12] \qquad (10)$$

$$\text{Reflectance, } R = \frac{(n-1)^2}{(n+1)^2}, \ [12] \qquad (11)$$

where n is the Refractive Index.

$$I = I_0 e^{-\mu x},\ \mu = -\frac{\ln \frac{I}{I_0}}{x} \quad [14] \qquad (12)$$

where μ is the Linear Total Attenuation Coefficient.

CALCULATION OF MICROSCOPIC OPTICAL PROPERTIES

The relevant formulas for microscopic calculations of absorption coefficient, scattering coefficient, reduced scattering coefficient, total attenuation coefficient and effective penetration depth are as follows.

The Kubelka-Munk Function is given by

$$F(R) = \frac{(1-R)^2}{2R} = \frac{k}{s}, \ [15] \qquad (13)$$

where R = Reflectance, k= Absorption Coefficient, s=Scattering Coefficient.

The total attenuation coefficient is described by

$$\mu = \mu_t = \mu_a + \mu_s, \quad [16] \qquad (14)$$

Where μ_a is Absorption Coefficient, and μ_s is Scattering Coefficient.

That is, k=μ_a and s=μ_s can be matched by using (13) and (14) formulas.

The reduced scattering coefficient (μ_s') is defined by the following equation;

$$\mu_s' = (1-g)\mu_s, \quad [17] \qquad (15)$$

Where g is the anisotropy factor. The g value of the phantom was fixed at 0.9, which is the anisotropy factor of human tissue in the UV and Near-Infrared spectra.

The effective penetration depth, D_{eff}, is described by the following formula;

$$D_{eff} = \frac{1}{\sqrt{3\mu_a[\mu_a+\mu_s(1-g)}}, \quad [18] \qquad (16)$$

RESULTS AND DISCUSSION

Acoustical Characterization Results

The acoustical properties of the tissue-mimicking materials made from Agar and Zerdine ® materials were determined as follows:

Sound Velocity Measurement Results

The Pulse-Eco method was utilized to measure the speed of ultrasonic waves in the materials. The results of the sound velocity measurements, obtained from this method, are presented in Figure 8.

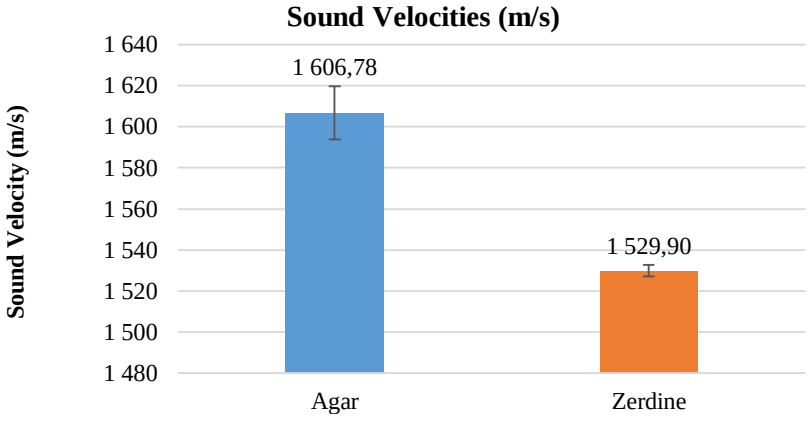

Fig. 8. Sound Velocities of Agar and Zerdine Phantoms.

Attenuation Coefficient Measurement Results

The Transmission technique was employed to measure the attenuation coefficient, which is a measure of how much ultrasonic waves will diminish as they pass through the tissue. The results of the attenuation coefficient measurements, obtained from this method, are shown in Figure 9.

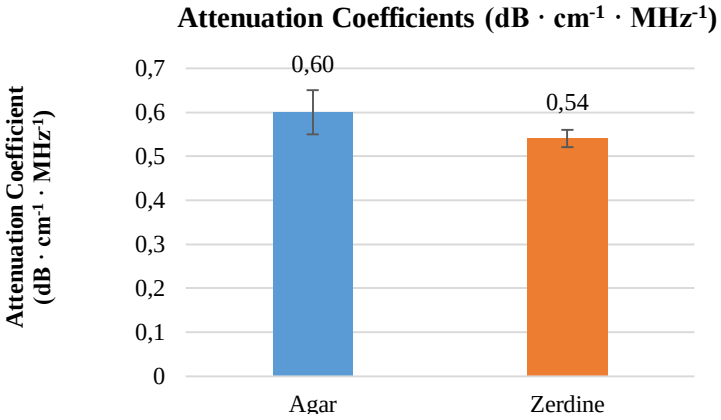

Fig. 9. Attenuation Coefficients of Agar and Zerdine Phantoms.

Density Measurement Results

The densities of the produced phantoms were calculated and are displayed in Figure 10.

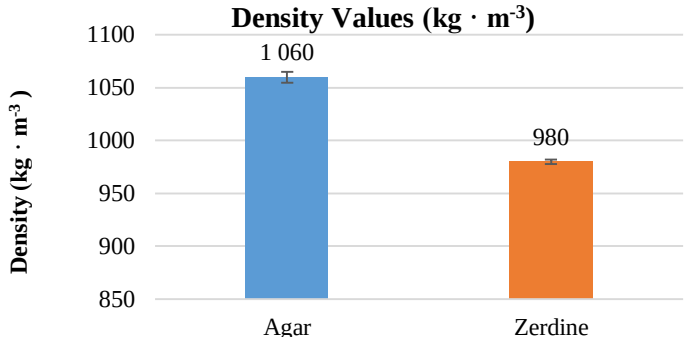

Fig. 10. Densities of Agar and Zerdine Phantoms.

Calculated Acoustic Impedance Values

The densities of the produced phantoms and the acoustic impedance values calculated using the sound velocity measurements are presented in Figure 11. The standard deviations for the acoustic impedance values were found to be very small and thus, are not included in the graph.

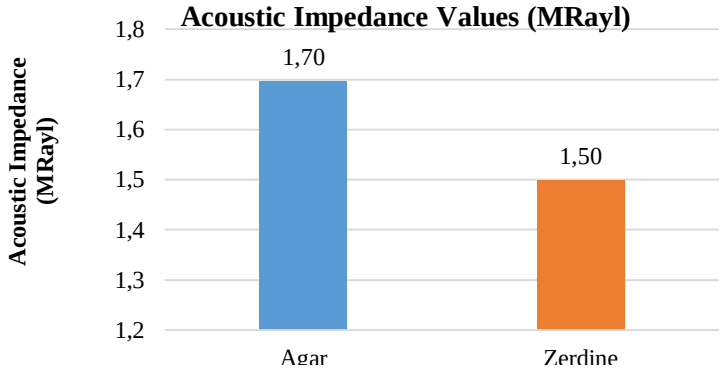

Fig. 11. Calculated Acoustic Impedances of Agar and Zerdine Phantoms

A summary of all the acoustical parameters obtained for the Agar and Zerdine phantoms through this study are presented in Table I.

Table I

Acoustic parameters determined for two different tissue-mimicking materials

TMM	Agar	Zerdine®
Sound Velocity ($m \cdot s^{-1}$)	1606.78 ± 13.00	1529.90 ± 2.86
Attenuation Coefficient ($dB \cdot cm^{-1} \cdot MHz^{-1}$)	0.6 ± 0.05	0.54 ± 0.02
Density ($kg \cdot m^{-3}$)	1060 ± 5	980 ± 2
Acoustic Impedance* (MRayl)	1.696	1.499

* Since the standard deviations calculated for acoustic impedance are very small, they are not given in the table.

Measurement Results of Macroscopic Optical Properties

The macroscopic optical properties, such as absorbance, transmittance, reflectance, refractive index, and attenuation coefficient, of the soft tissue phantoms were measured and calculated using the single integrating sphere test setup as reported in Table II and Table III in a previous study.

Table II

The measured macroscopic optical properties of the Zerdine and Agar phantom as average with the single integrating sphere measurement method

Phantom	Transmittance, T	Absorbance, A	Reflectance, R
Zerdine	0.91 ± 0.03	0.04 ± 0.01	0.05 ± 0.01
Agar	0.44 ± 0.21	0.41 ± 0.27	0.15 ± 0.09

Table III

The calculated macroscopic optical properties of the Zerdine and Agar phantom as average with the single integrating sphere measurement method

Phantom	Refractive Index	Total Attenuation Coefficient (cm^{-1})
Zerdine	1.58 ± 0.08	0.03 ± 0.01
Agar	2.26 ± 0.64	0.91 ± 0.10

Calculations of Microscopic Optical Properties

The microscopic optical properties of the soft tissue phantoms, including the absorption coefficient, scattering coefficient, reduced scattering coefficient, total attenuation coefficient, and effective penetration depth, were determined using the results from the single integrating sphere test setup. The calculated values for these properties are presented in Table IV and Table V.

Table IV

The calculated microscopic optical properties of the Zerdine and Agar phantom as average.

Phantom	Absorption Coefficient, μ_a, cm^{-1}	Scattering Coefficient, μ_s, cm^{-1}	Reduced Scattering Coefficient, μ_s', cm^{-1}
Zerdine	0.025 ± 0.011	0.003 ± 0.001	0.001 ± 0.0004
Agar	0.642 ± 0.074	0.266 ± 0.031	0.053 ± 0.006

Table V
The calculated total attenuation coefficient and effective penetration depth of the Zerdine and Agar phantom as average.

Phantom	Total Attenuation Coefficient, μ_t, cm^{-1}	Effective Penetration Depth, D_{eff}, cm
Zerdine	0.028 ± 0.012	22.655 ± 12.253
Agar	0.908 ± 0.104	0.865 ± 0.101

CONCLUSION

In this research, the acoustical and optical properties of two distinct tissue-mimicking materials, Zerdine and Agar, were studied and characterized. Acoustical properties such as density, sound velocity, and acoustic attenuation coefficient were measured using the Pulse-Echo method and transmission technique. Optical properties were studied using a single integrating sphere system and the Kubelka-Munk function approach. Macroscopic properties such as absorbance, transmittance, reflectance, refractive index, and attenuation coefficient were measured and calculated. Microscopic properties such as absorption coefficient, scattering coefficient, the reduced scattering coefficient, total attenuation coefficient, and effective penetration depth were calculated. The results of these studies provide a foundation for future research on the characterization of various phantoms.

[1] *E. Cetin, B. Karaboce, H.O. Durmus.* "Doku – Benzeri Malzemelerin Akustik Parametrelerinin Belirlenmesi." In 13. Ulusal Akustik Kongresi ve Sergisi, TAKDER.

[2] *Çetin, Emel, Hüseyin Okan Durmuş, Baki Karaböce, and Nuran Kavakli.* 2019. "Acoustical Characterization of Tissue - Mimicking Materials." Medical Measurements and Applications, MeMeA 2019 - Symposium Proceedings: 1–5.

[3] IEC 1390, Technical Report Type 21996. Ultrasonics-Real-Time Pulse-Echo Systems-Guide for Test Procedures to Determine Performance Specifications.

[4] IEC TS 62791:2015 ed: BSI. 2015. Ultrasonics - Pulse-Echo Scanners - Low-Echo Sphere Phantoms and Method for Performance Testing of Gray-Scale Medical Ultrasound Scanners Applicable to a Broad Range of Transducer Types.

[5] *Durmus, Huseyin Okan et al.* 2020. "Investigation of Basic Optical Properties of Tissue Phantoms under 635 Nm Low-Level Laser Irradiation." IEEE Medical Measurements and Applications, MeMeA 2020 - Conference Proceedings: 2–7.

[6] Dictionary, McGraw-Hill. "McGraw-Hill Dictionary of Scientific & Technical Terms, 6E, Copyright © 2003 by The McGraw-Hill Companies, Inc."

[7] *A.B. Murphy.* 2006. "Modified Kubelka-Munk Model for Calculation of the Reflectance of Coatings with Optically-Rough Surfaces." Journal of Physics D: Applied Physics 39(16): 3571–81.

[8] *Vargas, E. William, and A. Gunnar Niklasson.* 1997. "Applicability Conditions of the Kubelka–Munk Theory." Applied Optics 36(22): 5580.

[9] *Yang, Li, and Bjorn Kruse.* 2004. "Revised Kubelka – Munk Theory . I . Theory." J. Opt. Soc. Am. 21(10): 1933–41.

[10] *M. B. Zerhouni and M. Rachedine.* 1993. "Ultrasonic Calibration Material and Method,"

[11] *Karaböce, Baki et al.* 2018. "Investigation of Different TMMs in High Intensity Focused Ultrasound Applications." MeMeA 2018 - 2018 IEEE International Symposium on Medical Measurements and Applications, Proceedings.

[12] *M. Y. Nadeem, & W. Ahmed.* 2000. "Optical Properties of ZnS Thin Films." Turkish Journal of Physics 24(5): 651–59.

[13] *D.T. Harvey.* 2003. Analytical Chemistry for Technicians. ed. 3rd. John Kenkel.

[14] *Chang, Shuang, and Audrey K. Bowden.* 2019. "Review of Methods and Applications of Attenuation Coefficient Measurements with Optical Coherence Tomography." Journal of Biomedical Optics 24(09): 1.

[15] *J. O. S. E. Torrent, V. Barrón.* 2008. "Diffuse Reflectance Spectroscopy." In Methods of Soil Analysis, ed. April L. Ulery L. Richard Drees. , 367–85.

[16] *B.C. Wilson.* 1995. "Measurement of Tissue Optical Properties: Methods and Theories." In Optical-Thermal Response of Laser-Irradiated Tissue, Springer, Boston, MA., 233–303.

[17] *Jeong, Eun ju et al.* 2017. "Fabrication and Characterization of PVCP Human Breast Tissue-Mimicking Phantom for Photoacoustic Imaging." Biochip Journal 11(1): 67–75.

[18] *S.T. Flock, S. L. Jacques, B.C. Wilson, W. M. Star, & M. J. Van Gemert.* 1992. "Optical Properties of Intralipid: A Phantom Medium for Light Propagation Studies." Lasers in surgery and medicine 12(5): 510–19.

Received: 29.03.2023

CHANGE IN THE PHOTOLUMINESCENCE PROPERTIES OF STAIN ETCHED POROUS SILICON AFTER POSTTREATMENT IN VARIOUS ACID AND ALKALINE ETCHANTS

F.A. RUSTAMOV, N.H. DARVISHOV, V.E. BAGIEV, M.Z. MAMEDOV, E.Y. BOBROVA, H.O. ASKEROVA

Condensed Matter Physics Division, Institute for Physical Problems, Baku State University, Baku AZ 1148, Azerbaijan

E-mail: farhad.rustamov@bsu.edu.az

The effect of posttreatment in aqueous solutions of HF, KOH, NaOH and Na_2SeO_3 on the photoluminescence spectra of stain etched porous silicon has been investigated. It is shown that this posttreatment of as-prepared samples leads to a shift of the photoluminescence maximum from ~1.85 eV to 2.1 eV. Subsequent atmospheric oxidation during 2÷3 min leads to the transformation of the spectra, and its maximum shifts back to 1.85 eV. The intensity of photoluminescence after posttreatment of porous silicon depends on the composition of the etchant. In the HF solution, the photoluminescence intensity hardly changes, while in alkaline solutions it decreases. This is due to the different etching rates of silicon and silicon oxide in different etchants. The role of oxygen bonds in the formation of local radiative recombination levels in the band-gap, responsible for photoluminescence transformations, is discussed.

Keywords: porous silicon; stain etching; posttreatment; diluted HF; alkaline solutions; yellow PL; oxygen bonds
PACS: 81.40.−z; 78.67. Rb; 78.55.−m

1. INTRODUCTION

The phenomenon of visible photoluminescence (PL) in porous silicon (PS) has been intensively studied from both a practical and theoretical point of view since its discovery [1, 2]. From a practical point of view, this material has potential possibilities of practical application in micro- and optoelectronics, photovoltaics, biomedicine, as chemical and biological sensors, antireflection coating for solar cells, and so on [3, 4]. From a theoretical point of view, it is of interest to find out the physical mechanism of this phenomenon [5, 6]. Being an indirect-gap semiconductor with a band gap of 1.1 eV and with a lot of dangling bonds on the surface, a bulk crystal doesn't exhibit visible PL. After electrochemical or purely chemical etching, the transformed material, called porous silicon, begins to exhibit visible luminescence with a maximum higher than 1.1 eV. At present, it has been established that this is primarily due to the quantum size effect broadening the band gap in silicon nanocrystallites, which are obtained during the technological process of PS formation. And indeed, especially at small porosities, its observed that with an increase in porosity, i.e. with a decrease in the size of silicon nanocrystallites, a shift of the maximum PL to the high - energy region is observed [3, 4, 7]. But only the quantum-size effect cannot explain all observed experimental facts. In particular, at high porosities, the further shift of the PL maximum to the high - energy region stops [3, 4]. This experimental fact can be explained by the appearance, due to surface states, of radiative recombination levels located in the band gap. Theoretical works indicate that these levels arise during the oxidation of silicon crystallites [5, 6]. İt is shown, that when hydrogen bonds Si-H are replaced by oxygen bonds Si-O, local levels appear in the band gap of PS. Moreover, depending on the formation method of PS, this substitution can occur both during PS formation [8-11] and during atmospheric oxidation after formation [12-14]. It is the appearance of such radiative recombination levels that leads to red - orange photoluminescence, regardless of the porosity and size of silicon nanocrystals.

The PS samples, obtained by stain etching, are usually highly porous, and oxygen bonds in them are formed in the process of the formation of porous silicon in the etching solution [11]. As a consequence, instead of band-to-band transitions, transitions through these local levels prevail here. As a result, stain-etched porous silicon, regardless of porosity, exhibits stable red-orange or orange PL immediately after preparation. To shift the PL maximum in these PS samples, it is necessary to remove these oxygen bonds.

As is known, the silicon surface is well etched with aqueous solutions of HF and alkalis. But the effects of these solutions are different from each other. Depending on the type of etchant, its concentration, and etching duration, postetching can lead to the removal of oxygen bonds, a further reduction in the size of Si nanocrystallites, as well as to etching of the silicon itself, and a decrease in the thickness of the PS layer. Therefore, the final result of the effect of posttreatment on the maximum and intensity of PL requires further experimental research and comparative analysis.

In this work, we studied the effect of posttreatment on the PL spectra of stain etched porous silicon in HF, KOH, NaOH and Na_2SeO_3 solutions of various concentrations.

2. EXPERIMENT

Porous silicon samples were obtained by stain etching on p-type monocrystalline silicon substrates with a resistivity of 0.1 Om·cm and (111) orientation. To remove contaminant and degrease the surface, the plates were immersed in acetone for 50 min and then washed with bidistilled water. Then, to remove the

131, H.Javid ave, AZ-1143, Baku
Institute of Physics
E-mail: jophphysics@gmail.com

oxide layer, the surface of the plates was treated in a 10% aqueous HF solution for 1 min and then in concentrated HF (50%) for 5 min [19]. PS layers were formed at room temperature under daylight illumination in an HF(50%):HNO_3(65%):CH_3COOH (glacial) modified solution in a volume proportion of 1200:1:800, i.e., at oxidant insufficiency [20]. After the incubation time, the reaction of PS formation lasted 9 min. Such samples have a porosity of more than 70%, with crystallite sizes of 1.5÷2.8 nm [9, 21, 22]. Some of the samples immediately after the formation of PS were washed in bidistilled water and then was treated in various acid and alkaline etchants. It was very important to prevent contact of the PS with atmospheric air when transferring the obtained sample from the cleaning solution to the etching solution. PS samples were postetched in the following etchants: 10% aqueous solution of HF, NaOH, KOH and Na_2SeO_3 aqueous solutions in 0.0001M, 0.001M, 0.01M and 1M concentration within 1÷60 minutes. Then the samples were washed in bidistilled water, isopropyl alcohol and dried by N_2 jet. Immediately after drying, the PL spectra of the obtained samples were studied under ambient atmospheric conditions.

The PL spectra have been investigated at room temperature. The PL was excited by a Xenon lamp DKSL-1000, passed through an SPM-2 monochromator, and was recorded with an IKS-12 monochromator in the reflection geometry. In PL measurements, the excitation wavelength was 320 nm.

3. RESULTS

Fig.1 shows the PL spectra of stain etched PS samples both immediately after formation (a) and after posttreatment (b) in an alcohol solution of 10% HF in a volume proportion of 1:1. An alcohol solution was used to increase wettability. As can be seen from the figure, the samples that have not undergone additional treatment exhibit red PL with a peak at ~1.85 eV (Fig.1a).

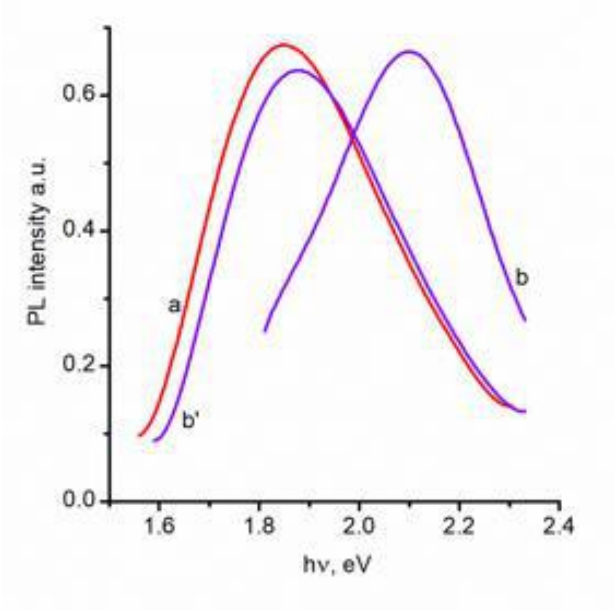

Fig.1. PL spectra of stain etched PS without and with posttreatment in dilute HF. a) as-prepared PS without postetching; b) as-prepared PS immediately after postetching in dilute HF; b') postetched PS after 5 min exposure in air.

This is a common PL spectrum observed in relatively highly porous PS samples obtained by conventional electrochemical or stain etching methods without posttreatment. Those samples that were subjected to posttreatment in an alcohol solution of 10% HF for ~ 10 min immediately after formation exhibit yellow PL with a maximum at 2.1 eV (Fig.1b). I.e. such additional etching of PS samples leads to a shift of PL peak to high-energy region (Fig.1, transition a → b). Upon contact with air, this PL spectrum is transformed very quickly (1 ÷ 3 min) and its maximum shifts back to ~ 1.85 eV (Fig.1, transition b→b'). As can be seen from Fig.1 the PL spectra of untreated samples and samples posttreated in an alcohol solution of 10% HF and exposed in air for more than 5 min practically coincide. Further exposure in air leads to a slight increase in the PL intensity without shifting its maximum.

Fig. 2 depicts the characteristic PL spectra of PS samples after 2 minutes of posttreatment in aqueous solutions of KOH of various concentrations. The PL spectra of PS samples subjected to posttreatment in aqueous solutions of NaOH and Na_2SeO_3 are not given because of their similarity to the spectra in Fig.2. As can be seen from the PL spectra, the posttreatment of PS samples in alkaline etchants also leads to a shift of the PL maximum to the high-energy region (Fig.2, transition a → b), i.e., red PL (~1.85 eV) turns into yellow (~2.1 eV). However, as shown in Fig. 2b, there is a significant decrease in intensity compared to the previous case's additional treatment in diluted HF in Fig. 1b.

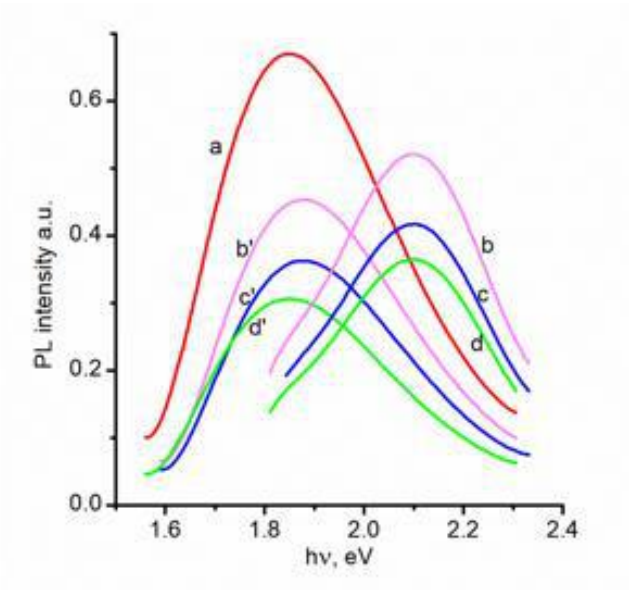

Fig.2. PL spectra of stain etched PS without and with posttreatment in KOH solutions. a) as-prepared PS without postetching; b) and b') PS postetched in 0.001M KOH immediately and after 5 min exposure in air; c) and c') PS postetched in 0.01M KOH immediately and after 5 min exposure in air; d) and d') PS postetched in 1M KOH immediately and after 5 min exposure in air.

Further exposure to air, as in the previous case, leads to the reverse shift of the PL peak to the initial position of 1.85 eV, but with a significant decrease in the intensity (Fig.2, transition b → b'). The increase in the concentration of etching alkaline solution doesn't change the position of the corresponding maxima, and it only leads to a decrease in intensity at each stage (Fig.2, transitions c → c' and d → d').

4. DISCUSSION

The PL emission spectra shown in Fig.1a and Fig.2a correspond to stain etched PS without posttreatment. These are typical PL spectra of PS, with a maximum in the red - orange region. Such spectra are observed both in the electrochemical and stain etching methods of PS formation. The reason for such PL is a total manifestation of the quantum-size effect in silicon nanocrystallites and their surface oxidation. The quantum-size effect expands the band-gap and surface oxidation leads to the appearance of local levels of radiative recombination. In the case of low PS porosity when the sizes of silicon nanocrystals are larger than ~4nm, these local levels are located inside the conduction band and do not show up in the PL emission spectrum [5, 6]. In this case, PL is a consequence of radiative zone-to-zone transitions. As the size of nanocrystals decreases, the peak of the PL spectrum slightly shifts to the high-energy region. But when the PS porosity is high and the size of nanocrystals becomes smaller than ~ 4 nm, the local level associated with surface states is located inside the band-gap. And, because radiative recombination occurs at these local levels in this case, a further decrease in the size of silicon crystallites, resulting in an increase in the width of the band gap, does not cause a shift in the PL maximum [5, 9, 22]. Such spectra are observed both in the electrochemical and stain etching methods of PS formation. The difference in the PL spectra obtained by different methods manifests itself when they are oxidized in air immediately after their preparation. The PL spectra of PS samples in the first case are strongly transformed, while in the second case they are quite stable. Early Fourier spectral studies show that this is due to the oxygen bonds (Si-O-Si asymmetric stretching of interstitial oxygen in Si at the band of 1108 cm-1 and O3-SiH bending and stretching mode at 882 cm-1 and 2245 cm-1 absorption peaks) that are already formed during the PS formation process during stain etching [11, 13, 23,]. I.e. in these samples' local radiative recombination levels, located in the band-gap and associated with Si-O bonds, appear in the etchant solution as PS is formed. As a result, despite the size and porosity of silicon nanocrystallites (1.8-2.3 nm), as-prepared stain-etched PS exhibit only red-orange PL [21, 22].

A comparison of Fig.1 and Fig.2 shows that, upon postetching of PS in various solutions of HF and KOH, a similar transformation of the PL spectra occurs. In all cases, the posttreatment leads to a significant shift of the PL maximum from 1.85 eV to 2.1 eV (a→b, a→c, a→d transitions). However, it should be kept in mind that such a shift can be detected only immediately after PS postetching, namely, only in as-prepared samples, until atmospheric oxidation affects. This similarity indicates the identity of the influence of various etchants on the PL mechanism. It is known that both dilute aqueous solutions of HF and alkaline aqueous solutions very quickly remove the oxide layer from the silicon surface [2, 5, 15 - 18]. Such a posttreatment of the samples in the above-mentioned etchants leads to the removal of Si-O bonds and, hence, to the removal of the local radiative levels located in the band-gap of silicon nanocrystallites. In the absence of these local levels in the band-gap, recombination occurs through band-to-band transitions, which is manifested in the

shift of the PL maximum from 1.85 eV to 2.1 eV. It should be noted that the position of the maximum of the PL spectrum (~2.1 eV) after postetching does not depend on the applied etchant, its concentration and the duration of postetching. Those, the limiting value of the maximum of the PL spectrum is always ~2.1 eV. Rather, this is the limiting value of the maximum PL which can be achieved in PC formed by electrochemical or stain etching methods [2, 13, 23, 24].

When exposed to atmospheric air, another similar transformation of the PL occurs (b→b', c→c', d→d' transitions). Within a few minutes, the PL peak reverse shifts from the yellow region (2.1 eV) to the low-energy red region (1.85 eV). This indicates the fact that silicon nanocrystallites are re-oxidized, which means that radiative recombination levels are again formed in the band-gap, leading to the observed shift of the PL peak. Radiative recombination proceeds again through these centers, regardless of the prehistory of sample processing.

The comparison of Fig.1 and Fig.2, in addition to the similarity in the shift of the PL maximum, also shows their difference in intensity behavior. The same reversible shift of the PL maximum red-yellow-red is observed after postetching PS in dilute HF solution or in alkaline KOH solutions followed by atmospheric oxidation. However, while after additional etching in HF solutions, the PL intensity remains almost unchanged, after additional etching in KOH solutions, the intensity noticeably decreases. Here, a different etching rate of silicon and its oxide in these etchants is manifested [2]. The posttreatment in a dilute HF solution for short etching times leads only to the removal of the oxide layer without changing the average size of Si nanocrystallites. In this case, the thickness of the luminescent layer almost does not change, and therefore the luminescence intensity also remains almost unchanged. In alkaline solutions, the etching rate of silicon and its oxide is high and grows with increasing concentration. As a result, when the PS is postetched in alkaline solutions, the thickness of the luminescent layer decreases, resulting in a reduction in PL intensity. Since the rate of PS etching increases with an increase in the concentration of KOH, the thickness of the luminescent layer also decreases. Therefore, with an increase in the KOH concentration, the intensity of PL also decreases.

5. CONCLUSIONS

A comparative study of the effect of additional etching in various etchants on the photoluminescence of stain etched porous silicon was carried out. The PS layers were obtained on the Si wafers by stain etching in a $HF:HNO_3:CH_3COOH$ solution at oxidant insufficiency. Immediately after formation all PS samples exhibited red PL (~1.85 eV). All samples were subjected to posttreatment in a dilute HF solution and various alkaline solutions. It was revealed that such posttreatment of the investigated samples always leads to a shift in the maximum of their PL maximum from the red (1.85 eV) to the yellow (~2.1 eV). This shift is associated with the removal of oxide layers from the surface of Si nanocrystallites and leads to the removal of radiative recombination levels in the band-gap. The removal of these levels leads to the predominance of band-to-band transitions in the PL spectrum. When exposed to air, the PL spectra transformed within 2-3 minutes due to atmospheric oxidation, and the PL maximum shifted back to the red region (2.1 eV 1.85 eV). This proves the decisive role of oxygen bonds on the PS surface in the PL mechanism. Despite the similarity in the PL maximum behavior, the posttreatment with various etchants affects its intensity in a different way. After additional etching in a dilute HF solution, the PL intensity remains almost unchanged. The postetching in alkaline solutions leads to a decrease in the PL intensity, and the higher the concentration of the solution, the lower the PL intensity. Such a change in the PL intensity is related to the different etching rates of silicon itself in these etchants.

[1] *L.T. Chanham.* Silicon quantum wire array fabrication by electrochemical and chemical dissolution of wafer, Appl. Phys. Lett. 57 (1990) 1046-1048. https://doi.org/10.1063/1.103561

[2] *V. Lehmann, U. Gosele*. Porous silicon formation: A quantum wire effect, Appl. Phys. Lett. 58 (1991) 856-858. https://doi.org/10.1063/1.104512

[3] *V. Lehmann.* Electrochemistry of Silicon, Wiley VCH, New York, 2002.

[4] *L.T. Chanham.* Properties of porous silicon. EMIS Data Review Series No. 18, London, 1997.

[5] *C. Delerue, G. Allan, M. Lannoo.* Theoretical aspects of the luminescence of porous silicon, Phys. Rev. B 48, 15 (1993) 11024-11036. https://doi.org/10.1103/PhysRevB.48.11024

[6] *M.V. Wolkin, J. Jorne, P.M. Fauchet, G. Allan, C. Delerue.* Electronic States and Luminescence in Porous Silicon Quantum Dots: Phys. Rev. Lett. 82, 1 (1999) 197-200. https://doi.org/10.1103/PhysRevLett.82.197

[7] *F.A. Rustamov, N.H. Darvishov, M.Z. Mamedov, E.Y. Bobrova, H.O. Qafarova.* Porous silicon bandgap broadening at natural oxidation. J. Lumin. 131, 10 (2011) 2078-2082. https://doi.org/10.1016/j.jlumin.2011.05.040

[8] *Y.Q. Jia, L.Z. Zhang, J.S. Fu, B.R. Zhang, J.C. Mao.* Characterization of stain etched porous Si with photoluminescence, electron paramagnetic resonance, and infrared absorption spectroscopy, J. Appl. Phys. 74 (12) (1993) 7615-7617. https://doi.org/10.1063/1.354940

[9] *É. Vázsonyi, E. Szilágyi, P. Petrik, Z. Horvath, T. Lohner, M. Fried, G Jalsovszky.* Porous silicon formation by stain etching, Thin Solid Films. 388 (2001) 295-302. https://doi.org/10.1016/S0040-6090(00)01816-2

[10] *B. González-Díaz, R. Guerrero-Lemus,*

J. Méndez-Ramos, B. Díaz-Herreraa, V.D. Rodríguez. Gradual oxidation of stain etched porous silicon nanostructures applied to silicon-based solar cells. Sens. Actuators, A 150 (2009) 97–101 https://doi.org/10.1016/j.sna.2008.12.006

[11] *F.A. Rustamov, N.H. Darvishov, V.E. Bagiev, M.Z. Mamedov, G.M. Eyvazova, E.Y. Bobrova, H.O. Qafarova.* Reversible quenching of photoluminescence in stain etched porous silicon at HNO_3 posttreatment and role of oxygen bonds. J.Lumin. 195 (2018) 49-53. https://doi.org/10.1016/j.jlumin.2017.11.011

[12] *E. Kayahan*, The role of surface oxidation on luminescence degradation of porous silicon, Appl. Surf. Sci. 257(9) (2011) 4311-4316. https://doi.org/10.1016/j.apsusc.2010.12.045

[13] *N. Arad-Vosk, A. Sa'ar.* Radiative and nonradiative relaxation phenomena in hydrogen- and oxygen-terminated porous silicon, Nanoscale Research Letters. 9, 47 (2014) 1-6. https://doi.org/10.1186/1556-276X-9-47

[14] *E. Galeazzo, A. Beltran, F. J. Ramirez-Fernandez.* Natural Oxidation of Porous Silicon, Brazilian Journal of Physics, 27/ A, 4, (1997) 170-172.

[15] *K.-H. Li, C. Tsai, J. Sarathy, J.C. Campbell.* Chemically induced shifts in the photoluminescence spectra of porous silicon. Appl. Phys. Lett. 62, 24 (1993) 3192-3194. https://doi.org/10.1063/1.109126

[16] *K. Murakoshi, K. Uosaki.* X-ray photoelectron spectroscopic studies of the chemical nature of as-prepared and NaOH-treated porous silicon layer. Appl. Phys. Lett. 62, 14 (1993) 1676-1678. https://doi.org/10.1063/1.109597

[17] *Y. Fukuda, W. Zhou, K. Furuya, H. Suzuki.* Photoluminescence change of as-prepared and aged porous silicon with NaOH treatment. J. Electrochem. Soc., 146, 7 (1999) 2697 – 2701. https://doi.org/10.1149/1.1391994

[18] *Y. Mo, A. Ren, J. Mao, Z. Zhou, H. Yuan, J. Du, D. Xiao.* Photoluminescence of oxidized porous silicon treated by sodium borohydride aqueous solution. Materials Letters75 (2012) 115 – 117. https://doi.org/10.1016/j.matlet.2012.01.130

[19] *F.A. Rustamov, N.H. Darvishov, V.E. Bagiev, M.Z. Mamedov, E.Y. Bobrova, H.O. Qafarova,* Influence of final treatment on the incubation period and antireflection properties of stain-etched porous silicon. Phys. Status Solidi. A 210, 10 (2013) 2174-2177. https://doi.org/10.1002/pssa.201329298

[20] *F.A. Rustamov, N.H. Darvishov, M.Z. Mamedov, E.Y. Bobrova, H.O. Qafarova,* Formation of lateral homogeneous stain etched porous silicon with acetic acid at oxidant insufficiency, Azerb. J. Physics. 18, 3 (2012) 44-49. http://inis.iaea.org/search/search.aspx?orig_q=RN:44023241

[21] *G. Di Francia, A. Citarella.* Kinetic of the growth of chemically etched porous silicon. J. Appl. Phys. 77 (7) (1995) 3549–3552. https://doi.org/10.1063/1.358585

[22] *F.A. Rustamov, N.H. Darvishov, V.E. Bagiev, M.Z. Mamedov, E.Y. Bobrova, H.O. Qafarova.* Determination of size and bandgap distributions of Si nanopaticles from photoluminescence excitation and emission spectra in n-type stain etched porous silicon, J. Lumin., 154 (2014) 2024-2028. https://doi.org/10.1016/j.jlumin.2014.04.037

[23] *X. Wen, P. Zhang, T.A. Smith, R.J. Anthony, U.R. Kortshagen, P.Yu, Y. Feng, S. Shrestha , G. Coniber, S. Huang.* Tunability limit of Photoluminescence in colloidal silicon nanocrystals. Sci. Rep. 5, (2015) 12469-12479. https://doi.org/10.1038/srep12469

[24] *K. Dohnalova, A. Poddubny, A. Prokofiev, W. Boer, C. Umesh, J. Paulusse, H. Zuilhof, T. Gregorkiewicz.* Surface brightens up Si quantum dots: direct bandgap-like size-tunable emission. Light Sci. Appl. 2, e47 (2013); 1-6. https://doi.org/10.1038/lsa.2013.3

Received: 10.04.2023

EFFECT OF ELECTRIC DISCHARGE PLASMA ON THERMOPHYSICAL PROPERTIES OF HDPE-BN COMPOSITES

T.D. IBRAGIMOV, G.Kh. HUSEYNOVA, Z.A. DADASHOV, A.F. NURALIYEV
Institute of Physics, Ministry of Science and Education of Azerbaijan
131, H. Javid ave., Baku, AZ 1143
tdibragimov @mail.ru

The effect of dielectric barrier discharge plasma before and after modification on thermo-physical properties of composites based on high density polyethylene and boron nitride particles was studied. It has been established that with an increase in the volume fraction of the filler, the entropy and enthalpy decrease, except for 3vol.% and 7 vol.%. The entropy and enthalpy increase after the plasma while the critical temperature almost does not change. The degree of crystallinity decreases after plasma treatment.

Keywords: boron nitride, high density polyethylene, dielectric barrier discharge plasma; difference of enthalpy and entropy of composites, crystallinity.
PACS: 77.84.Lf, 77.65.-j

INTRODUCTION

Surface modification by electric discharge plasma is one of the most interesting applications compared with other techniques which require vacuum conditions. Under electric discharge plasma treatment, the polymeric surface undergoes a functionalization process which includes the formation of various polar groups containing oxygen [1-2]. Authors of the work [3] used the corona discharge plasma technique to modify the properties of low density polyethylene film. The results obtained show good treatment homogeneity and an improvement of adhesion properties by the functionalization and etching of the film surface. In the work [4], low pressure glow discharge O2 plasma has been used in order to improve adhesion properties and make it useful for technical applications of low-density polyethylene (LDPE) film using differential scanning calorimetry. The results show that low pressure O2 plasma improves wettability in LDPE films and no significant changes can be observed at longer exposure times. The fluorine-containing polymer composite filled with piezo-ceramics were prepared by a hot pressing method in the work [5]. The significant increase of the surface energy and its polar component of polyethylene porous films were observed. The LDPE films modified by barrier discharge plasma were investigated to improve surface properties and adhesion of LDPE in the work [6/8]. It was shown that the topography of modified LDPE was significantly changed and the surface of modified polymer exhibited higher roughness in comparison with unmodified polymer. In the paper [7] plasma processing of polymer films and particles is examined by coating and noncoating plasmas. The authors believe that the difference by a factor of three in the etching rate between films in ammonia plasma is the consequence of their quasi-crystalline arrangement, compared to the amorphous PE films. In the paper [8], modification of the surface properties of PE films is studied using air dielectric barrier discharge plasma at atmospheric pressure. It is shown that air plasma can dramatically improve the wettability of PE surfaces. High-density polymer composites with semiconductor or dielectric fillers were prepared by the hot pressing method [9,10-15]. The results of the study indicate that, with increasing filler volume fraction, the thermal conductivity of the samples also increased.

Hexagonal boron nitride (h-BN) has high thermal conductivity and chemical stability [16-17]. It is widely used in engineering and refractory industries. Its high chemical resistance, high thermal resistance, high electrical resistance, lubricity, lightness, and high thermal conductivity are the superior properties of the hexagonal boron nitride and the reason of broad application areas [18].

The goal of this work to study of the effect of dielectric barrier discharge plasma on thermophysical properties of high density polyethylene doped with BN particles.

2. MATERIALS AND METHODS

We used high density polyethylene (HDPE) as a matrix. Melting and softening points of polymer are 130-135˚C and 80-90˚C, correspondingly. The hexagonal boron nitride particles with sizes of 2÷8 μm were added into the fine powder of polyethylene with different concentrations (3 vol. %, 5 vol. %, 7 vol. %, 10 vol. %, 15 vol.% and 20 vol.%). Then obtained mixture was shaken in a vortex mixer for 1 hour at room temperature, followed by sonication with dispergator Ultrasonic Cleaner NATO CD-4800 (China) for 4 hours. Disc-shaped samples of composites were obtained by hot pressing at temperature of 165˚C and pressure of 15 MPa. Pressing time after reaching the selected temperature is 15-20 minutes. The diameter and thickness of the obtained films were 4 cm and 100 μm, respectively. The electric discharges were used as non-thermal non-equilibrium plasma, which is termed surface micro-discharges (SMD). The generation of SMDs at ambient pressure is obtained from the dielectric-barrier discharge (DBD) technology which is related to the corona discharge family. The DBD treatment

131, H.Javid ave, AZ-1143, Baku
Institute of Physics
E-mail: jophphysics@gmail.com

carried out on the set up described earlier in the work [19-21]. In this case, the voltage of electric charge in the cells equals 8 kV. The plasma is created in an air layer of 2.5 mm. The exposure time of electric gas discharge plasma is taken to be 0.5 hours.

The differential scanning calorimeter DSC 204 F1 (firm Netzsch, Germany) with the CC200 F1 cooling system regulating the flow of liquid nitrogen was used to determine thermophysical parameters. Argon was served to purge and to protect the cell at the pressure of 50 kPa. The DSC204F1 and Proteus Analysis software programmes were used to process the results. The rate of temperature change was 10 K/min in the temperature range between 200C and 1500C. Exposure time was 30 min.

The critical temperature Tcr, at which the composite changes from one state to another, is determined by the local maximum of the heat flow while the change in enthalpy ΔH is determined by the expression

$$\Delta H = k \cdot \Delta A, \quad (1)$$

where k is coefficient characteristic of this device, A is the area under the corresponding peak. The entropy change ΔS during transition is defined as

$$\Delta S = \frac{\Delta H}{T_{cr}}, \quad (2)$$

The degree of crystallinity K is found according to the expression:

$$K = \frac{\left|\Delta H_h + \Delta H_c\right|}{\Delta H(100\% cryst)} 100\%, \quad (3)$$

where ΔHh and ΔHc are changes of enthalpy at heating and cooling processes, correspondingly;

ΔH (100 % cryst) is the change of enthalpy at 100% crystallites of matrix. For high-density polyethylene, the enthalpy change at 100% crystallization is taken to be equal to 293 J/g.

3. RESULTS AND DISCUSSION

Figure 1 shows DSC curves for both pure polymer and composites with different filler concentrations before and after discharge treatment.

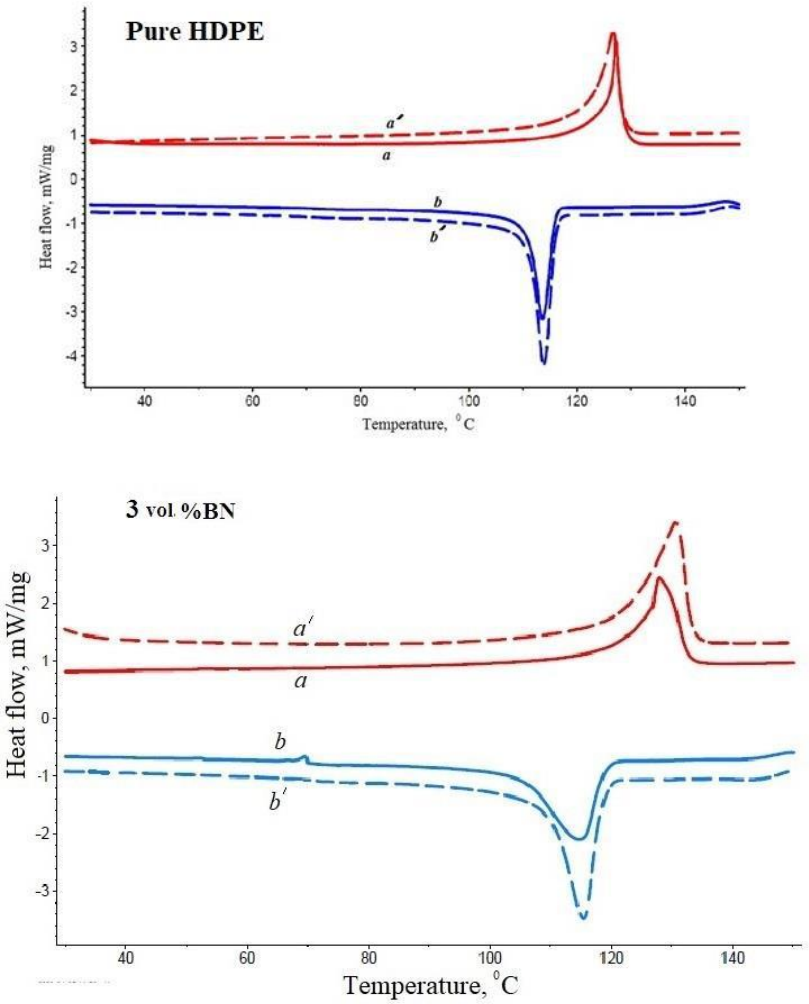

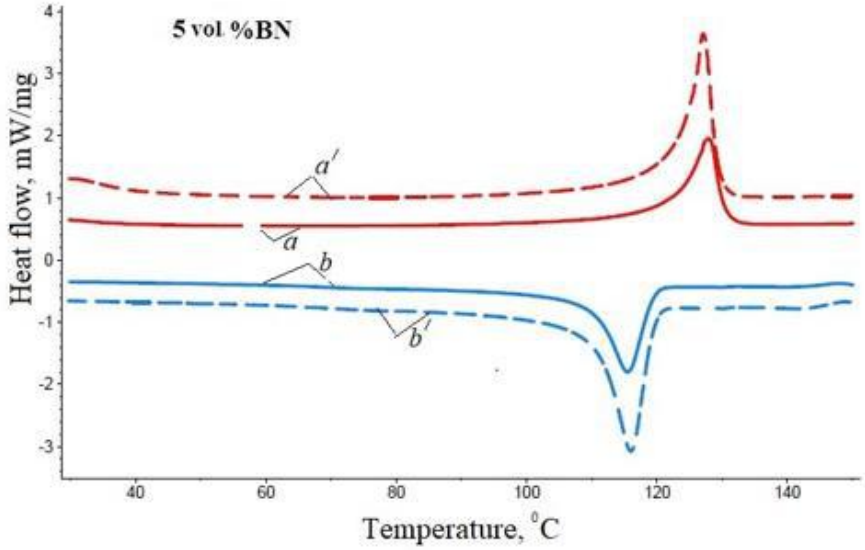
5 vol. %BN
Heat flow, mW/mg
Temperature, °C
a′
a
b
b′

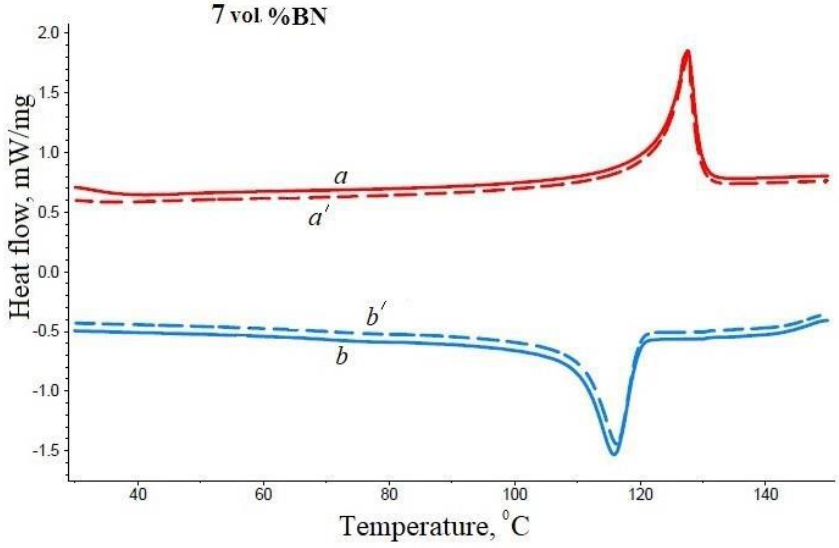
7 vol. %BN
Heat flow, mW/mg
Temperature, °C
a
a′
b′
b

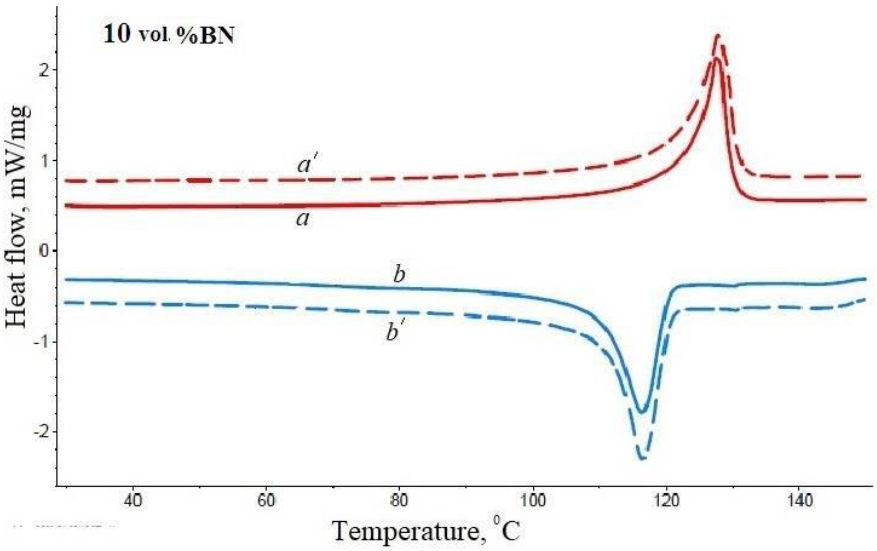
10 vol. %BN
Heat flow, mW/mg
Temperature, °C
a′
a
b
b′

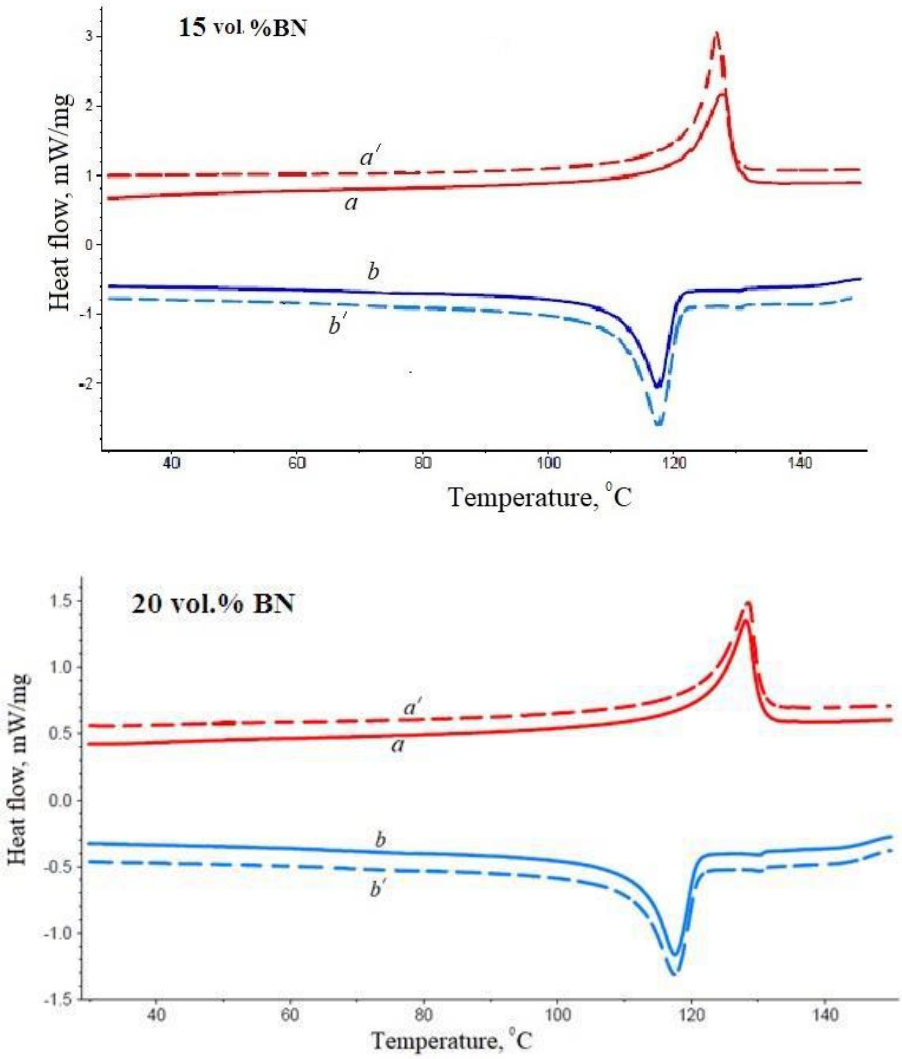

Fig. 1. Heat flow versus temperature for composites at various filler concentrations: (a) untreated sample at heating regime, (a′) plasma treated sample at heating regime, (b) untreated sample at cooling regime, (b′) plasma treated sample at cooling regime.

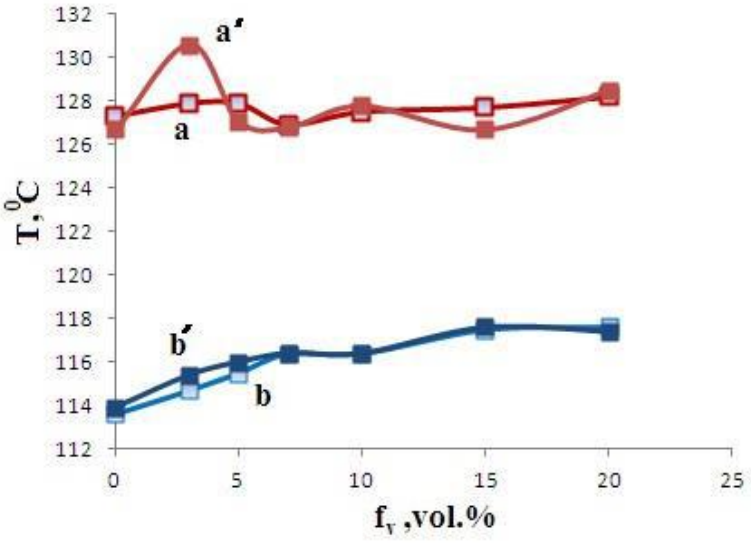

Fig 2. Dependence of critical temperature on filler concentration: (a) untreated sample at heating regime, (a′) plasma-treated sample at heating regime, (b) untreated sample at cooling regime, (b′) plasma-treated sample at cooling regime.

As can be seen from the DSC thermogram curves, the glass transition does not observe for pure polymer as well as composites. There are only peaks corresponding to transition from solid state to liquid one and vice versa. The peaks of the curves corresponding to cooling regime shifts to low temperatures. This indicates that the transition to the solid state of the composite occurs at lower temperatures. To more clearly determine the change for different filler concentrations, we plot the dependence of the critical temperature Tcr on the filler concentration and scanning regime. The corresponding curves are shown in Figure 2.

As can be seen, melting temperature as well as solidification one almost do not change except for the composite with concentration of 3 vol.% after plasma modification. Probably, the increase in the critical temperature at concentration of 3 vol. % is associated with a more uniform distribution of particles in the polymer matrix. At cooling regime, a higher concentration of filler induces the transition to solid state at higher temperatures.

Figure 3 shows the dependence of the change in enthalpy on the filler concentration during melting and solidification of the samples.

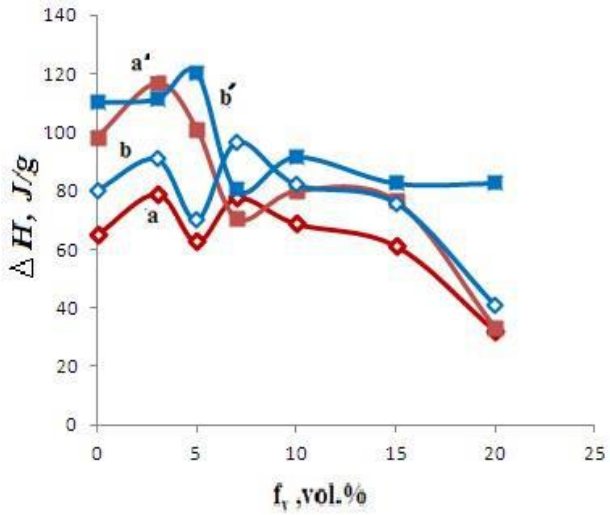

Fig. 3. The dependence of the change in enthalpy on the volume concentration of the filler during melting and solidification of the samples: (a) untreated sample at heating regime, (a′) plasma-treated sample at heating regime, (b) untreated sample at cooling regime, (b′) plasma-treated sample at cooling regime.

The enthalpy of the exothermic transition corresponding to melting according to the given volume fractions increases after the plasma modification. This is observed by the increase in the areas of the peaks shown in the figure. This is explained by the fact that more energy is required to activate the limited segmental movements of polymer chains after plasma modification.

As can be seen, the change in enthalpy during melting and solidification decreases with increasing filler concentration. At the same time, it is sharper at low concentrations while it is slower at high concentrations. The values of the enthalpy change during the solidification process at the same filler concentrations are less than during the melting process. In addition, gas discharge treatment of the samples increases the enthalpy change.

It is known that the enthalpy of fusion (melting) of a substance is the energy that is absorbed as heat from the body when it changes from solid state to liquid state (an exothermic process) and it occurs without raising the temperature for crystalline substances. It serves to disorganize the intermolecular bonds that hold molecules together. During curing, the reverse process (endothermic) occurs in which heat is removed from the substance. In this case, intermolecular bonds are restored, and the temperature does not change. For crystalline substances, the change in enthalpy during melting and solidification has the same value. The degree of crystallinity of polymers is small, so the above regularities do not apply to them [22]. Enthalpy is an extensive quantity, that is, for a composite system; it is equal to the sum of the enthalpies of its independent parts. Likewise, the enthalpy change of the composite is also the sum of the matrix and filler changes. The total change in the enthalpy of barium titanate particles is small, associated with a change in the symmetry group near the same temperature. But the volume fraction of the matrix, which has a sharp change in enthalpy, decreases. Therefore, the overall enthalpy change of the composite is reduced. These conclusions are in good agreement with the experimental curves of the change in enthalpy as a function of concentration.

The used technique of the barrier discharge plasma modifies the composite not only on the surface, but also in the bulk. This type of discharge is accompanied by the formation of accelerated electrons and ions, recombination radiation, active gas products and the appearance of surface electron-ion effects. The process occurs as a consequence of some breaks on the polymer chain; this situation allows the occurrence of some phenomena such as cross-linking, free radical formation, etc., with dramatic effects on the final

performance of polymeric materials. The surface of composites could be oxidized when it is exposed to oxygen environment. According to [6, 21, 23], additional oxidized species appear and oxygen atomic concentration increases. In particularly, ketone [−(C=O)−] and acetal [−(O−C−O)−] carbons are formed while the latter represents carboxyl [−(C−O)−O−] carbon. The formation of new connections contributes to the increase in the crystallinity of the composite. This corresponds to the experimental curves of crystallinity depending on the concentration (Fig. 4). At the same time, the decrease in the degree of crystallinity before and after processing is associated with a decrease in the volume fraction of polyethylene with an increase in the volume concentration of the filler.

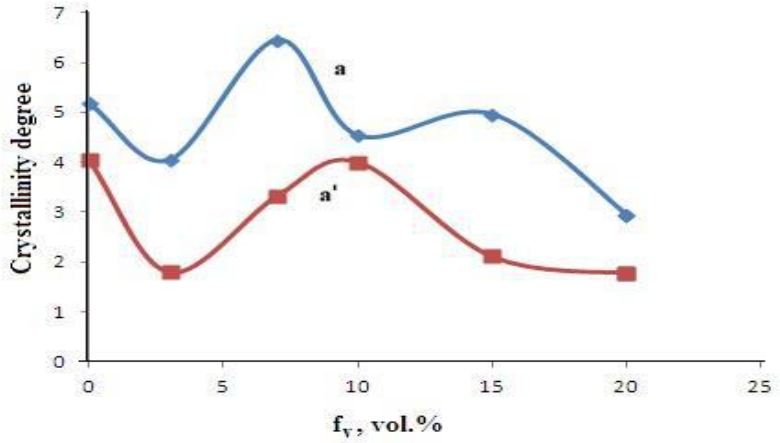

Fig. 4. Dependence of the degree of crystallinity on the volume concentration of the filler before (a) and after (a′) action of the gas discharge.

The results obtained show that the degree of crystallization decreases after plasma modification leading to an increase in the degree of amorphous. An increase in the degree of amorphous leads to the formation of stronger coordination bonds between the polymer and BN due to the breaking of the polymer chain during the plasma modification. The impact of electrical discharge plasma on BN also causes the destruction of its crystal lattice. Here, due to the influence of oxygen-containing groups, BN is split and its crystal structure is destroyed. As a result, B2O3 with an amorphous structure is formed. It can be seen from the graph obtained that the degree of crystallization decreases after plasma modification [24]. It can be explained by the formation of a new group with an amorphous structure in the composite.

4. CONCLUSIONS

It is shown that the critical temperature practically does not change during heating and cooling except for 3 vol.% after plasma modification. With an increase in the filler concentration, the volume fraction of the matrix decreases, which causes a change in the entropy and degree of crystallinity. In addition, there is an increase in entropy and enthalpy during plasma modification, as well as a decrease in the degree of crystallinity due to the formation of new bonds due to the influence of oxygen-containing groups. The particles decrease the degree of crystallinity developed within the matrix due to the constriction in the mobility of the polymer chains.

[1] *J.M. Grace and L.J. Gerenser.* Plasma treatment of polymers, J. Dispersion Sci. Technol. 24, 2003. 305-341.

[2] *S. Guimond and M.R. Wertheimer.* Surface degradation and hydrophobic recovery of polyolefins treated by air corona and nitrogen atmospheric pressure glow discharge, J. Appl. Polym. Sci. 94 (3), 2004. 1291-1303.

[3] *M. Pascual, R. Sanchis, L. Sánchez, D. García, and R. Balart.* Surface modification of low density polyethylene (LDPE) film using corona discharge plasma for technological applications, Journal of Adhesion Science and Technology 22, 2008. 1425–1442.

[4] *M.R. Sanchis, V. Blanes, M. Blanes, D. Garcia, R. Balart.* Surface modification of low density polyethylene (LDPE) film by low pressure O2 plasma treatment, European Polymer Journal 42 (7), 2006. 1558-1568.

[5] *L. Paralı.* The electret effects of crystallized polymer–ferropiezoelectric composite under electric discharge plasma, Journal of Electrostatics, 76, 2015. 89-94.

[6] *I. Novak, M. Steviar, A. Popelka, I. Chodak, J. Mosnacek, M. Spırkova´, I. Janigova, A. Kleinova, J. Sedliacik, M. Slouf.* Surface Modification of polyethylene by diffuse barrier discharge plasma. Polymer Engineering and Science. 2012. 1-8.

[7] *F. Arefi-Khonsaria, M. Tatouliana, F. Bretagnola, O. Bouloussab, F. Rondelez.* Processing of polymers by plasma

technologies. Surface & Coatings Technology 200, 2005. 14 – 20.

[8] *W. Kun, L. Jian, R. Chunsheng, W. Dezhen, W. Younian.* Surface modification of polyethylene (PE) films using dielectric barrier discharge plasma at atmospheric pressure. Plasma Science and Technology, 10 (4), 2008. 433-437.

[9] *L. Parali, M.A. Kurbanov, A.A. Bayramov, F.N. Tatardar, I.S. Ramazanova, G.X. Huseynova.* Effects of electric discharge plasma treatment on the thermal conductivity of polymer–metal nitride/carbide composites. Journal of Electronic Materials 44 (11), 2015. 4322–4333.

[10] *I. Novák, G.K. Elyashevichb, I. Chodák, A.S. Olifirenko, M. Števiar, M. Špírková, N. Saprykina, E. Vlasova, A. Kleinová.* Polymer matrix of polyethylene porous films functionalized by electrical discharge plasma, European Polymer Journal 44, 2008. 2702–2707.

[11] *M. Tahara, N.K. Cuong, Y. Nakashima.* Improvement in adhesion of polyethylene by glow-discharge plasma. Surface and Coatings Technology, 174–175 (2003) 826-830.

[12] *R. Morent, N. De Geyter, T. Jacobs, S. Van Vlierberghe, P. Dubruel, C. Leys, E. Schacht.* Plasma-polymerization of HMDSO using an atmospheric Pressure dielectric barrier discharge plasma process. Polym. 6 (2009) 537–542.

[13] *H. Biederman, D. Slavínská.* Plasma polymer films and their future prospects. Surface and Coatings Technology. 125(1–3) (2000) 371-376.

[14] *M.A. Kurbanov, V.A. Gol'dade, S.V. Zotov, I.S. Ramazanova, A.F. Nuraliev, F.F. Yakhyaev, U.V. Yusifova, B.G. Khudayarov.* Generation of craze-formation centers in polymer films under the action of electric discharge plasma. Technical Physics 63 (2018) 965–969.

[15] *A.I. Drachev, A.B. Gil'man.* The synthesis of semiconducting polymers in a low-temperature plasma. Russian Journal of Physical Chemistry A, Focus on Chemistry 82 (2008) 1733–1741.

[16] *A. Akay, O. Durukan, Y. Göncü, A. T. Seyhan, N. Ay.* Hexagonal boron nitride filled polymer nanofibers producing and characterization via electrospinning technique. Akay et al. Usak University Journal of Material Sciences, 1 (2012) 35 – 41.

[17] *L. Chen, H. Xu, Sh. He, Y Du.* Thermal conductivity performance of polypropylene composites filled with polydopamine-functionalized hexagonal boron nitride. journal.pone. 0170523 January 20, 2017.1-16

[18] *Y. Yang, Y. Peng, M. F. Saleem.* Hexagonal boron nitride on III–V compounds: A Review of the Synthesis and Applications. Materials, 15, 2022. 4396

[19] *F. Truica-Marasescu, M.R. Wertheimer.* Nitrogen-rich plasma-polymer films for biomedical applications plasma process. Polym. 5 (2008) 44–57.

[20] *P.-L. Girard-Lauriault, P. Desjardins, Wolfgang E.S.Unger, A.Lippitz, M.R. Wertheimer.* Chemical characterisation of nitrogen-rich plasma-polymer films deposited in dielectric barrier discharges at atmospheric pressure plasma process. Polym. 5 (2008) 631–644.

[21] *M.A. Kurbanov, I.S. Sultanakhmedova, É.A. Kerimov, Kh.S. Aliev, G.G. Aliev, and G.M. Geidarov.* Plasma crystallization of polymer–ferroelectric/piezoelectric ceramic composites and their piezoelectric properties. Physics of the Solid State, 51 (6) (2009) 1223–1230.

[22] *Z.M. Cinan, T. Baskan, B. Erol, S. Mutlu.* Thermal conductivity and phase change properties of boron nitride-lead oxide nanoparticles doped polymer nanocomposites. Research Squae. Turkey (2022)3-49.

[23] *Y. Kusano.* Atmospheric pressure plasma processing for polymer adhesion: a review. The Journal of Adhesion, 90 (2014) 755–777.

[24] *P. Carminati, S. Jacques, F. Rebillat.* Oxidation/corrosion of BN-based coatings, as future BN-based interphases for SiC/SiC composites. Journal of the European Ceramic Society, (2020) 03011733-1-24.

Received: 11.04.2023

DIELECTRIC RELAXATION OF ABSORPTION SPECTRA OF ISOPROPYL, n-BUTYL AND ISOBUTYL ALCOHOLS IN MICROWAVE RANGE

S.T. AZIZOV
Institute of Physics of Ministry of Science and Education, H. Javid ave.,131, Baku, Azerbaijan
e – mail: samir_azizov@mail.ru

The investigation results of dielectric constant ε′ and absorption coefficient ε″ of isopropyl, n-butyl and isobutyl alcohols at wave lengths 3,22; 1,80 and 1,15 sm in temperature interval from –50°C up to +50°C are given in the article. The dielectric relaxation of absorption spectra of isopropyl, n-butyl and isobutyl alcohols is studied. It is shown that all studied objects of high-frequency dielectric constants $\varepsilon_{\infty,2}$ of the additional absorption region have the bigger value than the square of the optical refractive index.

Keywords: dielectric spectroscopy, dielectric relaxation, dielectric constant, isopropyl alcohol, n-butyl alcohol, isobutyl alcohol.
PACS: 61.20. – p; 77.22. – d; 77.22.Gm;

INTRODUCTION

Nowadays, it is established that the dispersion low-frequency region of the electromagnetic waves in the prime aliphatic alcohols can be well described by the unique time of the dielectric relaxation in big temperature intervals [1]. Besides, the data proving the presence of additional absorption regions [2] are obtained. However, these data are limited and related to supercooled state because of which the problem of additional absorption stays open. According to [2,3] at room temperatures this absorption should be observed in the range of centimeter and millimeter waves where as it is known the carrying out of measurements is connected with the big technical and method difficulties.

The main aim of the present investigation is the study of the some dielectric aspects of local structures of the some aliphatic alcohols in microwave range, and also the study of absorption spectrum dielectric relaxation in the big temperature intervals.

THE MATERIALS AND INVESTIGATION METHODS

The some data obtained for isopropyl, n-butyl and isobutyl alcohols are given in the present work. The dielectric constants ε' and dielectric losses ε" of these alcohols at wavelengths 3,22; 1,80 and 1,15 cm in temperature interval from 50 up to –50° C are measured. The measurements are carried out on installations made by us by Malov-Poly method [4,5,6]. The error for the values of dielectric constants ε' doesn't increase 2-3% and for the values of dielectric losses ε" doesn't increase 3-5%. The measurement cell temperature with the sample is supported with the help of the thermostat and the cuprum is measured by the constantan thermocouple with accuracy 0,3°C. The investigated compounds after rigorous purification and drying are treated by triple distillation on rectifying column.

INVESTIGATION RESULTS

The measurement results of temperature dependence of dielectric constants ε' and dielectric losses ε" for isopropyl, n-butyl and isobutyl alcohols are given in table 1.

Table 1

The temperature dependences of dielectric constants ε' and dielectric losses ε" for isopropyl, n-butyl and isobutyl alcohols

t °C	Isopropyl alcohol						n-butyl alcohol					
	3,22 см		1,80см		1,15см		3,22 см		1,80см		1,15см	
	ε'	ε"	ε'	ε"	ε'	ε"	ε'	ε"	ε'	ε"	ε'	ε"
50	3,55	1,68	3,28	1,40	3,10	1,26	3,26	1,24	3,05	1,04	2,88	0,94
40	3,46	1,38	3,25	1,17	3,04	1,07	3,21	1,04	3,01	0,90	2,83	0,87
30	3,38	1,13	3,21	0,96	3,00	0,90	3,18	0,87	2,96	0,80	2,80	0,77
20	3,33	0,94	3,18	0,81	2,96	0,78	3,14	0,75	2,92	0,70	2,77	0,68
10	3,30	0,79	3,16	0,70	2,92	0,67	3,10	0,66	2,88	0,63	2,73	0,61
0	3,27	0,66	3,12	0,61	2,88	0,59	3,06	0,58	2,86	0,55	2,70	0,52
– 10	3,24	0,57	3,09	0,54	2,84	0,52	3,02	0,52	2,83	0,49	2,69	0,47
– 20	3,22	0,50	3,07	0,51	2,81	0,46	2,98	0,46	2,80	0,44	2,64	0,43
– 30	3,20	0,45	3,05	0,47	2,78	0,43	2,94	0,44	2,77	0,41	2,62	0,39
– 40	3,18	0,41	3,03	0,44	2,77	0,42	2,91	0,42	2,74	0,39	2,59	0,37
– 50	3,17	0,38	3,01	0,42	2,76	0,41	2,90	0,41	2,72	0,37	2,57	0,34

131, H.Javid ave, AZ-1143, Baku
Institute of Physics
E-mail: jophphysics@gmail.com

t °C	Isobutyl alcohol					
	3,22 см		1,80см		1,15см	
	ε'	ε"	ε'	ε"	ε'	ε"
50	3,11	1,19	2,96	0,94	2,75	0,85
40	3,04	0,97	2,91	0,80	2,71	0,76
30	2,98	0,80	2,87	0,69	2,68	0,66
20	2,94	0,64	2,83	0,59	2,61	0,57
10	2,91	0,54	2,79	0,50	2,58	0,48
0	2,88	0,47	2,76	0,43	2,56	0,41
– 10	2,85	0,42	2,74	0,40	2,54	0,39
– 20	2,83	0,37	2,73	0,35	2,53	0,33
– 30	2,81	0,33	2,71	0,31	2,52	0,30
– 40	2,79	0,31	2,69	0,29	2,51	0,27
– 50	2,76	0,30	2,67	0,28	2,50	0,26

Supposing the additivity of contributions of the both dispersion regions into measured dielectric constants ε' and dielectric losses ε", it is easy to show that the values of dielectric coefficients corresponding to dispersion second region are defined by the following formulae:

$$\boldsymbol{\varepsilon_2^{'} = \varepsilon^{'} - \frac{\varepsilon_{0.1} - \varepsilon_{\infty,1}}{1+\left(f/f_{0,1}\right)^2}}\ ,\ \boldsymbol{\varepsilon_2^{"} = \varepsilon^{"} - \frac{\varepsilon_{0.1} - \varepsilon_{\infty,1}}{1+\left(f/f_{0,1}\right)^2}\left(f/f_{0,1}\right)} \qquad (1)$$

here $\boldsymbol{\varepsilon_{0,1}}$ and $\boldsymbol{\varepsilon_{\infty,1}}$ are the equilibrium and high-frequency dielectric constant of the dispersion main region correspondingly, $\boldsymbol{f_{0,1}}$ is critical frequency of this region, f is the frequency on which the measurement is done.

The parameter values of the main region of dispersion necessary for calculation corresponding with data in the limits of test errors [2] are given in table 2.

Table 2

The calculation values $\boldsymbol{\varepsilon_{0,1}}$ and $\boldsymbol{\varepsilon_{\infty,1}}$ of equillibrium and high-frequency dielectric constants of the main region of dispersion.

t °C	Isopropyl alcohol					n-butyl alcohol				
	$\varepsilon_{0,1}$	$\varepsilon_{\infty,1}$	$10^{-8}f_{0,1}$,Hz	$\varepsilon_{\infty,2}$	$10^{12}\tau$, sec	$\varepsilon_{0,1}$	$\varepsilon_{\infty,1}$	$10^{-8}f_{0,1}$,Hz	$\varepsilon_{\infty,2}$	$10^{12}\tau$, sec
30	17,3	3,39	5,52	2,11	3,8	16,6	3,35	3,41	2,12	5,5
20	18,6	3,43	4,00	2,12	4,0	18,1	3,38	2,46	2,13	6,3
10	20,0	3,45	2,77	2,14	4,3	19,6	3,41	1,62	2,16	7,3
0	21,4	3,48	1,71	2,16	4,8	21,2	3,44	1,06	2,18	8,4
– 10	23,0	3,52	1,05	2,18	5,6	22,6	3,48	0,69	2,20	9,9
– 20	24,7	3,56	0,663	2,20	6,5	24,3	3,53	0,43	2,22	12,5
– 30	26,4	3,59	0,389	2,22	7,5	26,0	3,56	0,25	2,25	15,1
– 40	28,5	3,65	0,215	2,25	9,3	27,9	3,59	0,145	2,27	19,4
– 50	30,7	3,70	0,110	2,28	10,8	29,8	3,64	0,080	2,30	24,0

Isobutyl alcohol				
$\varepsilon_{0,1}$	$\varepsilon_{\infty,1}$	$10^{-8}f_{0,1}$,Hz	$\varepsilon_{\infty,2}$	$10^{12}\tau$,sec
16,2	3,19	2,83	2,13	6,4
17,5	3,22	1,96	2,14	7,2
19,0	3,25	1,23	2,16	8,4
20,4	3,29	0,782	2,18	10,2
22,1	3,34	0,482	2,19	12,3
23,8	3,37	0,284	2,22	14,8
25,8	3,40	0,149	2,23	18,7
27,6	3,44	0,083	2,25	23,8
29,6	3,47	0,043	2,27	29,0

The further calculation is easy to carry out with the help of graphic method. Coal - Coal diagram [8,9] for the studied compounds at +20° and –20° C are shown in Fig.1.

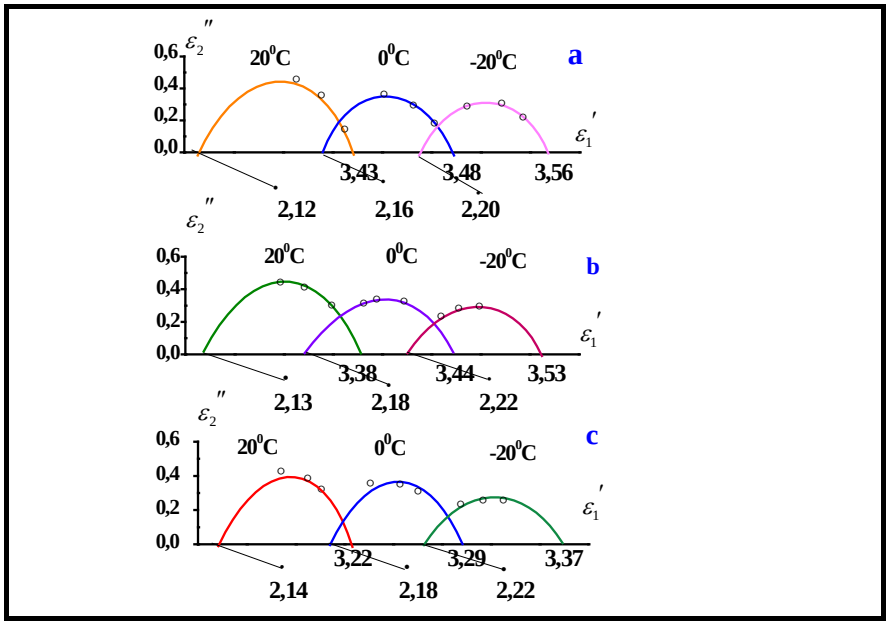

Fig.1. Coal-Coal diagrams: a is isopropyl alcohol; b is n-butyl alcohol; c is isobutyl alcohol.

RESULT DISCUSSION

At diagram construction it is shown that low-frequency limit of second region of absorption is equal to high-frequency limit of the main dispersion. As it is seen from the Fig.1 ε_2' and ε_2'' values calculated by formulae (1), are well lied on the semicircle arc with the center below X-axis that shows on the presence of symmetrical distribution of relaxation time near more probable one. The distribution increase is observed with the temperature decrease. The averaged relaxation times τ found from diagrams and also the high-frequency dielectric constants $\varepsilon_{\infty,2}$ of additional absorption region are given in table 2. The spread between values of relaxation time τ found on the different waves in average isn't more 10 – 15%. Such correspondence is well enough if we take under consideration the error of parameter distribution of main dispersion. The fact of the visible increase of the value of high-frequency dielectric constants $\varepsilon_{\infty,2}$ of addition absorption region under the value of square of optic refraction index of all studied objects attract attention because of which one can conclude the probable existence of one more high-frequency absorption region.

CONCLUSION

The microwave dielectric absorption in isopropyl, n-butyl and isobutyl alcohols in wide temperature interval is studied. The high-frequency dispersion region characterizing by the symmetrical distribution of dielectric relaxation time takes place in studied compounds. It is established that in all studied regions the values of high-frequency dielectric constants $\varepsilon_{\infty,2}$ of additional absorption region exceeds the values of the square of optic refraction index from which one can conclude the probable existence of one more high-frequency absorption region.

[1] *F. Kremer, A. Schonhals.* Broadband Dielectric Spectroscopy, Springer (2002) 729
[2] *I. Doroshenko, G. Pitsevich, V. Shablinskas.* Cluster structure of liquid alcohols: study by vibrational spectroscopy (2012) 290
[3] *Yu.A. Gusev.* Fundamentals of Dielectric Spectroscopy Tutorial Kazan KSU (2008) 112
[4] *S.T. Azizov, O.A. Aliev, R.G. Abaszade.* Low-frequency dielectric properties of the benzene-bromobenzene system AJP Fizika, (2019) volume XXV № 2 section: En, 3 – 5 http://physics.gov.az/physart/209_2019_02_03_en.pdf
[5] *C.J.F. Böttcher, P. Bordwijk,* Theory of Electric polarization, Amsterdam (1978) vol. 2
[6] *S.R. Kasimova,* Measurements of the Dielectric Properties of Strongly Absorbing Substances at Microwave Frequencies, Measurement Techniques. USA, New – York (2016) Vol.58, Is. 12,1372 – 1375. https://doi.org/10.1007/s11018-016-0901-9
[7] *A.Ju. Ahadov.* Dielectric parameters of pure liquids M. (1999) 854.
[8] *S.T. Azizov, G.M. Askerov.* Investigation of the equilibrium and dynamic characteristics

of the dielectric polarization of a chlorobenzene- n-butyl solution AJP Fizika (2020) volume XXVI №2 section: En, 15 – 17. http://physics.gov.az/physart/250_2020_02_17_en.pdf

[9] *S.R. Kasimova*. Measurement of dielectric properties of highly absorbing substances at microwave frequencies. Metrology Moscow Russia (2015) №4 60 – 65.

Received: 11.04.2023

LOSSES FOR PARAMETRIC INTERACTION IN MEDIUM WITH NEGATIVE REFRACTION

ASMAR RASIM AHMADOVA
Physics Department, Baku State University,
acad. Z. Khalilov str. 23, AZ1148, Baku, Azerbaijan
asmar.ahmadova.r@bsu.edu.az

An analytical expression was acquired for determining the optimal value of the pump intensity during three-wave interaction in medium with negative refraction under the condition of phase synchronism. The losses for parametric interaction in the metamaterial can be compensated for the backward wave. The optimal value for pumping intensity is obtained by analytical solution. The analysis showed that it depends on the intensity of interacting signal and idler waves.

Keywords: metamaterial, parametric interaction, negative refraction.
PACS: 42.65ky, 42.61b, 42.55.-f.

INTRODUCTION

The discovery of metamaterials contributed to the emergence of the possibility of controlling light radiation by changing the optical properties of such artificial structures. Resonant interactions, the existence of backward waves, negative refraction in chronological order were considered in the works of G. Lamb [1], L.I. Mandelstam [2], D.V. Sivukhin [3], V.N. Agranovich and V.L. Ginzburg [4], V.G. Veselago [5] and others. [6].

One of the features of these materials is the possibility within the same structure at the same time, but for different frequency ranges, to ensure the existence of both positive and negative values of the real part of the refractive index of a nonlinear medium (i.e., simultaneously negative values of the dielectric (ε dielectric permittivity) and magnetic permeability (μ magnetic permeability). Hence, the unconventional result of the interaction of an electromagnetic pump wave with a metamaterial manifests itself in the nonlinear interaction of optical waves, for example, in the generation of harmonics [7,8], as well as in the generation of sum and difference frequencies. Then, if the pump wave is in the frequency range with a negative refractive index, and the harmonic wave is in the frequency range with the opposite sign of the refractive index, then the fundamental wave transfers energy in the opposite direction to its phase velocity. With such a geometry, the pump wave is known to be a backward wave. In this case, the maximum intensity of the harmonic is achieved not at the output, but at the input to the nonlinear medium. This medium plays the role of a nonlinear mirror. A similar conduction of a nonlinear medium is manifested in the case of a degenerate four-wave interaction when observing the effect of wavefront reversal of laser radiation [9-11].

To date, thanks to the improvement of the technology of manufacturing metamaterials, their development from the radio range is moving towards the visible range. In [12] they report on the results of developments already in the near IR and in the visible ranges of the spectrum.

In the constant field approximation a theoretical study of the nonlinear optical interaction in such artificial structures was carried out in a number of works, of which we note [9–15, 16-23]. In the constant field approximation [15, 24, 31], we studied the generation of the second and third harmonics, the effects of self-action in a metamaterial [25, 26].

In classical electrodynamics, according to the dispersion relations of Kramers - Kronig, which determine the behavior of the optical constant of the medium - the real (refractive index) and imaginary (absorption coefficient) parts of the electrical permeability of frequency, at the resonant frequency, the absorption coefficient increases sharply, which leads to significant energy losses of the electromagnetic wave. Thus, there are inevitable losses in metamaterials that weaken the electromagnetic wave.

The main problem in the study of metamaterials is high losses. [7-10]. Various constructive variants of metamaterials are being investigated, where it is possible to attenuate signal losses. One of the ways to overcome the losses is considered and proposed as a result of the analysis in the constant intensity approximation [12] in the work [13,14]. The influence of losses in metamaterials for the case of four-wave interaction is studied for the process of amplification and generation of the reverse signal wave in the constant intensity approximation.

The aim of this scientific work is to study of phase effects in three-wave parametric interaction in metamaterials, and also to compute the optimal study of the pump intensity in a three-wave parametric interaction in a metamaterial. The nonlinear optical interaction in metamaterials has been studied in the constant intensity approximation [8,9]. In the constant intensity approximation the generation of the second and third harmonics, self-action effects and parametric interaction in metamaterials [27-30], four-wave interaction in metamaterials [24, 29] were studied.

THEORY

Consideration is carried out for the case of parametric three-wave interaction in a metamaterial at a frequency ω_p. We believe that the properties of the metamaterial are manifested for the wave at the pump

131, H.Javid ave, AZ-1143, Baku
Institute of Physics
E-mail: jophphysics@gmail.com

frequency ω_p ($\omega_p = \omega_i - \omega_s$). We assume that the waves at the frequencies of the signal and pump waves run along the positive z axis. In the constant intensity approximation, parametric interaction in a metamaterial without taking into account losses, but at different phase distances and initial values of the intensities of the interacting waves at high-frequency and low-frequency pumping, was carried out by us in [27, 28].

The usual shortened equations for three interacting waves in a metamaterial take the form [27]:

$$\frac{dA_i}{dz} + \delta_i A_i = -i\gamma_i A_s A_p e^{-i\Delta z}$$

$$\frac{dA_s}{dz} - \delta_s A_s = -i\gamma_s A_i A_p^* e^{i\Delta z} \quad (1)$$

$$\frac{dA_p}{dz} + \delta_p A_p = -i\gamma_p A_i A_s^* e^{i\Delta z}$$

Here, $A_{i,s,p}$ the corresponding complex amplitudes of the interacting waves, δ_j - are the absorption coefficients of the medium at frequencies ω_j (j=1,3),

$$\gamma_i = \frac{8\pi\chi_{eff}^{(2)}\omega_i^2\varepsilon_i}{k_i c^2}, \gamma_s = \frac{8\pi\chi_{eff}^{(2)}\omega_s^2\varepsilon_s}{k_s c^2}, \gamma_p = \frac{8\pi\chi_{eff}^{(2)}\omega_p^2\varepsilon_p}{k_p c^2}$$

- coefficients of nonlinear connection of waves at the corresponding frequencies, $\Delta = k_i - k_s - k_p$ - phase mismatch between interacting waves, $\chi_{eff}^{(2)}$- effective quadratic susceptibility of the medium, $z = 0$ corresponds to the entrance to the left of the metamaterial.

When constructing the second equation of system (1), we took into account that the medium has a negative refractive index at the frequency ω_s, so a minus sign appears in front of the loss factor in the second equation.

The boundary conditions in this case are:

$$A_{i,p}(z=0) = A_{i0,p0}\,, A_s(z=l) = A_{sl}\,. \quad (2)$$

$A_{i0,p0}$ - the input values of the waves at the sum frequency and at the frequency of the pump wave at $z = 0$, A_{sl} the initial amplitude of the wave at the difference frequency ω_s at the entrance to the metamaterial on the right.

We apply the constant intensity approximation of the fundamental radiation, $I_{i,p}(z) = I_{i,p}(z=0) = const$ and for the intensity of the wave at the difference frequency ω_s at the output on the left at z=0 we obtain [30]:

$$I_s(z=0) = I_{sl}\frac{\exp\left[(\delta_i + \delta_p - \delta_s)l\right] + \frac{\gamma_s^2 I_{i0} I_{p0}^*}{I_{sl}}\left(\frac{\mathrm{sh}\lambda l}{\lambda}\right)^2}{\left[\mathrm{ch}\lambda l + \frac{(\delta_i + \delta_s + \delta_p)}{2}\frac{\mathrm{sh}\lambda l}{\lambda}\right]^2} \quad (3)$$

here,

$$\Gamma_p^2 = \gamma_i\gamma_s I_{p0},\ \Gamma_i^2 = \gamma_s\gamma_p I_{i0},\ I_{j0} = A_{j0}\cdot A_{j0}^*, j = 1 \div 3,\ \lambda = \sqrt{\Gamma_p^2 - \Gamma_i^2 + \frac{(\delta_i+\delta_s+\delta_p)^2}{4}}.$$

In order to study the optimal generation mode with respect to the intensity of a strong pump wave, we take the derivative of the output signal intensity on I_{p0}, i.e.,

$$\frac{dI_s}{dI_{p0}} = \frac{\left(\frac{\gamma_s^s I_{i0} I_{p0}^*}{I_{sl}}\right)'\left[\left(\frac{\mathrm{sh}\lambda l}{\lambda}\right)^2\right]'}{\left[\left(\mathrm{ch}\lambda l + \delta_s\frac{\mathrm{sh}\lambda l}{\lambda}\right)^2\right]'}$$

As a result of mathematical transformations, we obtain

$$a\cdot\left[\left(\frac{\mathrm{sh}\lambda l}{\lambda}\right) + sI_{p0}^*\cdot\lambda' b\right]\frac{\mathrm{sh}\lambda l}{\lambda}\cdot c = 2\left[1 + aI_{p0}^*\left(\frac{\mathrm{sh}\lambda l}{\lambda}\right)^2\right](\lambda' l\cdot\mathrm{sh}\lambda l + \delta_s\lambda' b)$$

$$a\cdot c\cdot\frac{\mathrm{sh}\lambda l}{\lambda} = \left[\left(\frac{\mathrm{sh}\lambda l}{\lambda}\right) + 2I_{p0}^*\cdot\lambda' b\right]s\lambda'\left[1 + aI_{p0}^*\left(\frac{\mathrm{sh}\lambda l}{\lambda}\right)^2\right](l\cdot\mathrm{sh}\lambda l + \delta_s b) \quad (4)$$

Where made are the following substitutions:

$$a = \frac{\gamma_s^2 I_{i0}}{I_{sl}}, b = \frac{\mathrm{ch}\lambda l \cdot \lambda l - \mathrm{sh}\lambda l}{\lambda^2}, c = \mathrm{ch}\lambda l + \delta_s \frac{\mathrm{sh}\lambda l}{\lambda}, \lambda' = \sqrt{\Gamma_p^2 - \Gamma_i^2 + \frac{(2\delta_s - i\Delta)^2}{4}}.$$

Here, to simplify the calculations, we assume that the real and imaginary input intensity values I_{p0} are equal, i.e. $I_{p0} = I_{p0}^*$. This does not limit the scope of the problem and does not significantly change the interaction analysis. By solving the right and left parts of the obtained analytical expression separately, it will be possible to numerically determine the optimal value of the intensity I_{p0} for each set of problem parameters (phase mismatch, wave losses and pump wave intensity (via the parameter Γ_p^2) and intensity of the direct wave (via the parameter Γ_i^2).
This calculation can be required in the development of parametric transducers based on metamaterials.

CONCLUSION

Thus, the paper considers, taking into account phase effects, the parametric interaction of waves in a quadratic medium, which is “left” for a signal wave. The features of the process in this case are analyzed. We performed an analytical calculation for the optimal value of the pump intensity for three-wave interaction in medium with negative refraction under the condition of phase matching. It is shown that the optimal value of the pump intensity depends on the intensities of the interacting signal and idler waves. This fact is not found in the constant intensity approximation. By analytically solving the obtained expression, one can calculate the optimal value of the pump wave intensity for each set of problem parameters (phase mismatch, wave loss, and pump wave intensity (via the parameter Γ_p^2) and direct wave intensity (via the parameter Γ_i^2).

This calculation can be required in the development of parametric transducers based on metamaterials.

[1] *H. Lamb.* On the Propagation of Tremors over the Surface of an Elastic Solid. Proc. London Math. Soc., V. 1, № 2 (1904) 473.

[2] *L.I. Mandelstam.* Lectures, lectured on February 26, 1940 and May 5, 1944. Full. coll. tr. 5. (*M.:* Proceedings of the Academy of Sciences of the USSR, 1950.

[3] *D.V. Sivuxin.* On the energy of an electromagnetic field in dispersive medium. Optics and Spectrum, V. 3 № 4 (1957) 308-314.

[4] *V.M. Agranovich and V.L. Ginzburg.* Crystal Optics Taking into Account Spatial Dispersion and Excitation Theory [in Russian], Izd. Nauka, Moscow, V. 5 № 2 (1965) 376-381.

[5] *V.G. Veselago.* The Electrodynamics of substances with simultaneously negative values of ε and μ. Sov. Phys. Usp., V. 10 № 4 (1968) 509-514.

[6] *A.N. Lagarkov, V.N. Kisel, A.K. Sarychev, V.N. Semenenko.* Теплофизика высоких температур, V. 6, № 48 (2010) 1031-1034.

[7] *A.K. Popov, S.A Myslivets., V.M. Shalaev.* Coherent Nonlinear-optical Energy Transfer and Backward-wave Optical Parametric Generation in Negative-index Metamaterials, V.405, № 7 (2010) 2999-3002.

[8] *S. Zhang, W. Fan, N.C. Panoiu, K. J. Malloy, R.M. Osgood and R.J. Brueck.* Experimental Demonstration of Near-Infrared Negative-Index Metamaterials. Phys. Rev. Lett., V. 95, № 13 (2005) 95-101.

[9] *N.G. Basov, I.G. Zubarev.* Phase conjugation of laser radiation. Nature, V. 405, № 8 (1980) 8-18.

[10] *J.F. Reinjes.* Nonlinear optical parametric processes in liquids and gases. Orlando, (1984) 478 pages.

[11] *Z.A. Tagiev, R.J. Kasumova, R.A. Salmanova.* Theory of degenerate four-wave mixing in the prescribed intensity approximation. Optics and Spectroscopy, V. 87, №1 (1999) 86-89.

[12] *Xiao Shumin, V.P. Drachev, A.V Kildishev, Ni Xingjie, U.K. Chettiar, Yuan Hsiao-Kuan, V.M. Shalaev.* Loss-free and active optical negative-index metamaterials. Nature, V. 466, № 7307 (2010) 735 - 738.

[13] *Jinggui Zhang, Yuanjiang Xiang, Lifu Zhang, Yongfan Li, and Zhaoming Luo.* Induced focusing of optical wave from cross-phase modulation in nonlinear metamaterials. IEEE Journal of Quantum Electronics, V. 10, № 50 (2014) 823-830.

[14] *I.V. Shadrivov, A.A.Zharov, Y.S. Kivshar.* Second-harmonic generation in nonlinear left-handed metamaterials, JOSA, V. 23, № 3 (2006) 529-534.

[15] *Z.H. Tagiev, R.J. Kasumova, R.A. Salmanova, N.V. Kerimova.* Constant-intensity approximation in a nonlinear wave theory. J. Opt. B: Quantum Semiclas. Opt., V. 3, № 3 (2001) P. 84 -87.

[16] *Zh. Kudyshev, I. Gabitov, and A. Maimistov.* Effect of phase mismatch on second-harmonic generation in negative-index materials Phys.Rev., V. 87, № 6 (2013) 063840

[17] *M. Scalora, M. A. Vincenti, D. De Ceglia, V. Roppo., M. Centini, N. Akozbek and M. J. Bloemer.* Second- and third-harmonic generation in metal-based structures. Phys.Rev., V. 82, № 4 (2010) 043828 [14 pages].

[18] *M. W. Klein, M. Wegener, N. Feth, S Linden.* Experiments on second- and third-harmonic

generation from magnetic metamaterials Optics Express, V. 15, № 8 (2007) 5238-5247

[19] *V.M. Agranovich, Y.R. Shen, R.H. Baughman., A.A. Zakhidov.* Linear and nonlinear wave propagation in negative refraction metamaterials. Phys. Rev., V.69, № 16 (2004) 1-7.

[20] *A.I. Maimistov, I.R. Gabitov.* Nonlinear optical effects in media with a positive-negative refractive index. Bulletin of the Russian Academy of Sciences: Physics, 72, № 3 (2008) 704-707.

[21] *A.B. Kozyrev, H. Kim., D.W. Weide.* Parametric amplification in left-handed transmission line media. Appl. Phys. Lett., 88, № 4 (2006) 264101-1

[22] *W.J. Padilla., D.N. Basov, D.R. Smith.* Negative refractive index metamaterials. Materials today, 9, №7-8, (2006) 28

[23] *W.J. Padilla, A.J. Taylor.* Dynamical Electric and Magnetic Metamaterial Response at Terahertz Frequencies. Phys. Rev. Lett., V. 96, № 10 (2006) 1401-4

[24] *R.J. Kasumova.* Four wave mixing and compensating losses in metamaterials. Superlattices and Microstructures, V. 61, № 3 (2018) 86-91.

[25] *Z.H., Tagiev, R.J. Kasumova, L.S. Gadjieva.* Phase effects at second-harmonic generation in metamaterials. Journal of Russian Laser Research, V. 32, № 2 (2011) 188-199.

[26] *R.J. Kasumova, G.A. Safarova, Sh.A. Shamilova, N.V. Kerimova.* Phase effects in metamaterials at Third-Harmonic Generation. International Journal of Engineering and Technology IJET-IJENS, V.15, №06 (2015) 19-30.

[27] *R.J. Kasumova, Sh.Sh. Amirov, Sh.A. Shamilova,* "Parametric interaction of optical waves in metamaterials under low-frequency pumping," Quantum Electron. V. 47, № 7 (2017) 655-660.

[28] *R.J. Kasumova, Z.H. Tagiyev, Sh.Sh. Amirov, Sh.A. Shamilova, G.A. Safarova.* Phase effects at parametrical interaction in metamaterials. Journal of Russian Laser Research, V. 18, № 1 (2017) 211 – 218.

[29] *R.J. Kasumova, G.A. Safarova, Sh.Sh. Amirov, A.R Akhmadova.* Four-wave mixing in metamaterials. Russian Physics Journal, Volume 61, № 9 (2019) 1559-1567.

[30] *R.J. Kasumova, N.V. Kerimova, G.A. Safarova, A.R. Akhmadova.* Compensation of losses at three wave parametric interaction in the matematerials. Newspaper "Baku State University", №1, (2020) 42-45.

[31] *Z.H. Tagiev, A.S. Chirkin.* "Fixed intensity approximation in the theory of nonlinear waves," Zh. Eksp. Teor. Fiz., V. 73, № 2 (1977) 1271-1282.

Received: 03.05.2023

CHANGE OF MESOGENIC PROPERTIES OF LIQUID CRYSTAL 5CB AT THE PRESENCE OF SILVER NANORODS

T.D. IBRAGIMOV, A.R. IMAMALIYEV, G.A. MURADOVA
Institute of Physics, Ministry of Science and Education of Azerbaijan
131, H. Javid ave., Baku, AZ 1143
tdibragimov @mail.ru

Influence of silver nanorods on mesogenic properties of nematic liquid crystal 4- cyano-40-pentylbiphenyl (5CB) is investigated by the methods of differential scanning calorimeter, polarization microscopy, and dielectric spectroscopy. It is shown that the temperature of the nematic-isotropic transition increases. In this case, there is a decrease in enthalpy and entropy of the phase transition at presence of silver nanorods.

Keywords: nematic liquid crystal; silver nanorods; polarization microscopy; differential scanning calorimetry; electric conductivity; dielectric permittivity.
PACS: 64.70.mj; 64.70.pv; 77.84.Nh; 82.70.Dd.

INTRODUCTION

One of the rapidly developing fields of physics is plasmonics. Plasmon resonance is very sensitive to the environment of corresponding nanostructures. Therefore, the possibility of changing the optical and dielectric properties of the medium is an effective way to control the surface plasmon resonance. Liquid crystals (LC) are suitable candidates for the role of such media.

Dispersion of small amount (0.02 wt.% and 0.05 wt.%) of silver nanoparticles (NP) in nematic LC increases cleaning temperature and the conductivity anisotropy while threshold voltage decreases [1]. It is shown in the work [2] that the existence of dipole–dipole correlation could be the main reason of decreasing of dielectric anisotropy at low concentration (0.25 wt.%) of silver NPs in LC. Methods of Raman spectroscopy and dielectric measurements show that the inclusion of silver NP (0.25 wt.% and 0.50 wt.%) in LC leads to the modification in molecular polarizability of LC and a decrease in magnitude of dielectric anisotropy [3]. Authors of the work [4] observed that the inclusion of small concentration (1 wt.%) of gold NPs into nematic LC decreases switch-on voltage and the relaxation frequency due to internal local electric field generated because of the relative permittivity differences of gold NPs and LC material. Thermodynamical, dielectric, optical and electro-optical characterisation of pure 8CB and its composites with gold and silver nanoparticles have been studied in the work [5]. It was shown that clearing temperature, threshold voltage for Freederick transition, switching voltage, splay elastic constant, and the optical band gap decrease while ionic conductivity, relaxation frequency and activation energy increase. Dielectric anisotropy is almost unchanged for both the nanocomposites. It is shown in the work [6] that the dispersion of Ag NPs (0.5 wt./wt.%, 1 wt./wt.% and 2 wt./wt.% (into nematic LC 4′-(Octyloxy)-4-biphenylcarbonitrile leads to the change in physical parameters such as dielectric permittivity, photoluminescence, threshold voltage, response time and splay elastic constant. The AC conductivity and threshold voltage of Ag NPs-dispersed composite system have increased significantly.

The liquid crystal 5CB doped with alkylthiol-capped gold NPs (0.1 -5 wt.%) has been investigated in the work [7]. It is shown that the nematic–isotropic transition of the composite decreases nearly linearly with increasing concentration of NP. At this case, the electrical conductivity of the system increases by more than two orders of magnitude.

The negligible change is observed in the value of birefringence for the lower doping concentration ($\leq$ 0.5 wt%) of silver nanorods in nematic LC by the authors of the work [8]. The parallel and perpendicular components of dielectric permittivity increase with the addition nanorods. The conductivity increases at the doping concentration of 0.2 wt% however decreases with further increase in the doping concentration because of the trapping of ionic impurities by of silver nanorods.

The aim of the work is to study mesogenic properties of liquid crystal 5CB at presence of silver nanorods.

EXPERIMENTAL

We used nematic liquid crystal 4-cyano-40-pentylbiphenyl (5CB) from the firm Merck with positive dielectric anisotropy as a matrix. The temperature range of the nematic phase of this LC is usually located between 21.3^0C and 35.2^0C.

The silver nanorods (US, Research Nanomaterials, In.) had diameters of 2-5 nm and lengths of 10-20 nm. They were dispersed into ethanol then the mixture was added into the liquid crystal. The obtained mixture was shaken in a vortex mixer for 6 hour at temperature 40^0C until the ethanol is completely evaporated, The resulting mixture with concentration of 0.2 wt.% was induced by sonication with dispergator Ultrasonic Cleaner NATO CD-4800 (China) for 4 hours.

The differential scanning calorimeter DSC 204 F1 (firm Netzsch, Germany) with the CC200 F1

131, H.Javid ave, AZ-1143, Baku
Institute of Physics
E-mail: jophphysics@gmail.com

cooling system regulating the flow of liquid nitrogen was used to determine thermo-physical parameters. Argon was served to purge and to protect the cell at the pressure of 50 kPa. The DSC204F1 and Proteus Analysis software program was used to process the results. The rate of temperature change was 5 K/min in the temperature range between 0^0C and 45^0C.

The critical temperature T, at which the composite changes from one state to another, was determined by the local maximum of the heat flow while the change in enthalpy ΔH was defined by the expression:

$$\Delta H = k \cdot \Delta A, \quad (1)$$

where k is characteristic for this device, A is the area under the corresponding peak. The entropy change ΔS during transition was defined as:

$$\Delta S = \frac{\Delta H}{T}. \quad (2)$$

The images of colloid textures were observed under the Carl Zeiss polarisation microscope (model 720, Germany).

Dielectric and conductivity measurements were carried out by the Precision LCR Meter 1920 (IET Labs. Inc., USA) at the frequency of 1 kHz and at temperature range between 22^0C - 45^0C. The cell had a sandwich structure and consisted of two plane-parallel glass plates whose inner surfaces were coated with thin transparent and conductive indium-tin-oxide (ITO) layer. Planar orientation of molecules was attained by coating the inner substrate surfaces with rubbed polyimide layers. For obtaining of homeotropic orientation of LC molecules, we used the surfactant (polysiloxane). The cell thickness was fixed with calibrated 20 μm polymer spacers for measurements. Both the colloid and the pure LC were injected into the empty cell by capillary action at the isotropic state. To increase the dispersion, the cells with the colloid were placed at electric field of 40V to achieve turbulence and were kept for 2 days. In this case, no aggregation of particles was observed. The filled cell was kept in the special heater with temperature regulator GL-100 (China). The copper-constantan thermocouple was used for temperature control. An accuracy of temperature determination was 0.1^0C. In such a case, applied voltage was 0.5V for both LC molecular orientations. Electric capacity C and dissipation factor (the loss tangent) *D* were recorded by means of this device at frequency *f* of 1 kHz. The magnitudes of dielectric permittivity *ε* were defined as:

$$\varepsilon = \frac{C}{C_0}, \quad (3)$$

where C_0 is the electric capacity of the empty cell. The real ε' and image ε'' parts of dielectric permittivity and electric conductance σ were calculated by the expressions:

$$\varepsilon' = \frac{\varepsilon}{\sqrt{1+D^2}}, \quad (4)$$

$$\varepsilon'' = \frac{\varepsilon D}{\sqrt{1+D^2}}, \quad (5)$$

$$\sigma = 2\pi f \varepsilon_o \varepsilon'', \quad (6)$$

RESULTS AND DISCUSSION

Figure 1 shows the DSC curves of both the pure LC and the colloid at heating and cooling regimes.

First, it can be seen from Fig. 1 that the pronounced DSC peak of the pure LC is observed at the heating regime, the maximum of which conforms with temperature of the transition from crystalline phase to LC one while the corresponding peak is weak at the cooling regime.

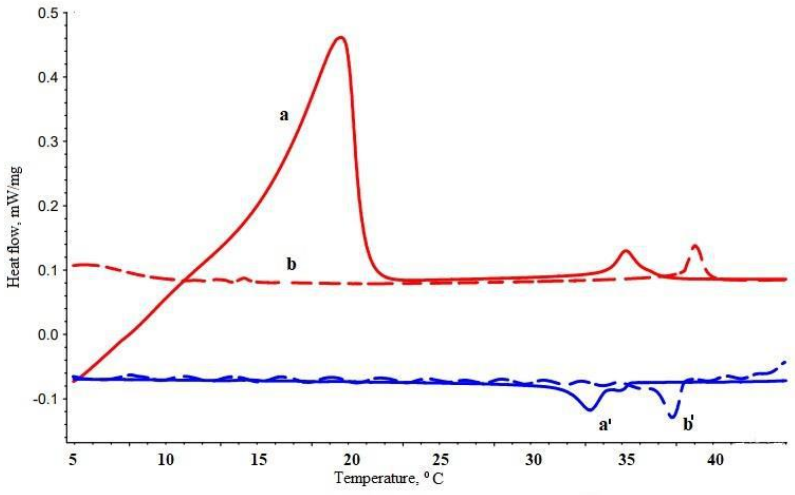

Fig.1. Dependence of heat flow on temperature: (a) the pure LC at heating regime; (a′) the pure LC at cooling regime; (b) the colloid at heating regime; (b′) the colloid at cooling regime.

The DSC peak of the transition from the crystalline to the liquid-crystalline state of the colloid is not observed at the investigated temperature range. It indicates that the presence of nanorods prevents the corresponding transition. The critical point of the phase transition from the LC state to the isotropic one shifts to higher temperatures at both the heating regime and the cooling regime with the additive of nanorods. Moreover, the transition temperature at cooling regime is lower relative to the heating one. It is obvious that there is overcooling of the material.

Figure 2 shows images under the polarizing microscope of both the pure LC and the colloid near the transition from the LC state to the isotropic one.

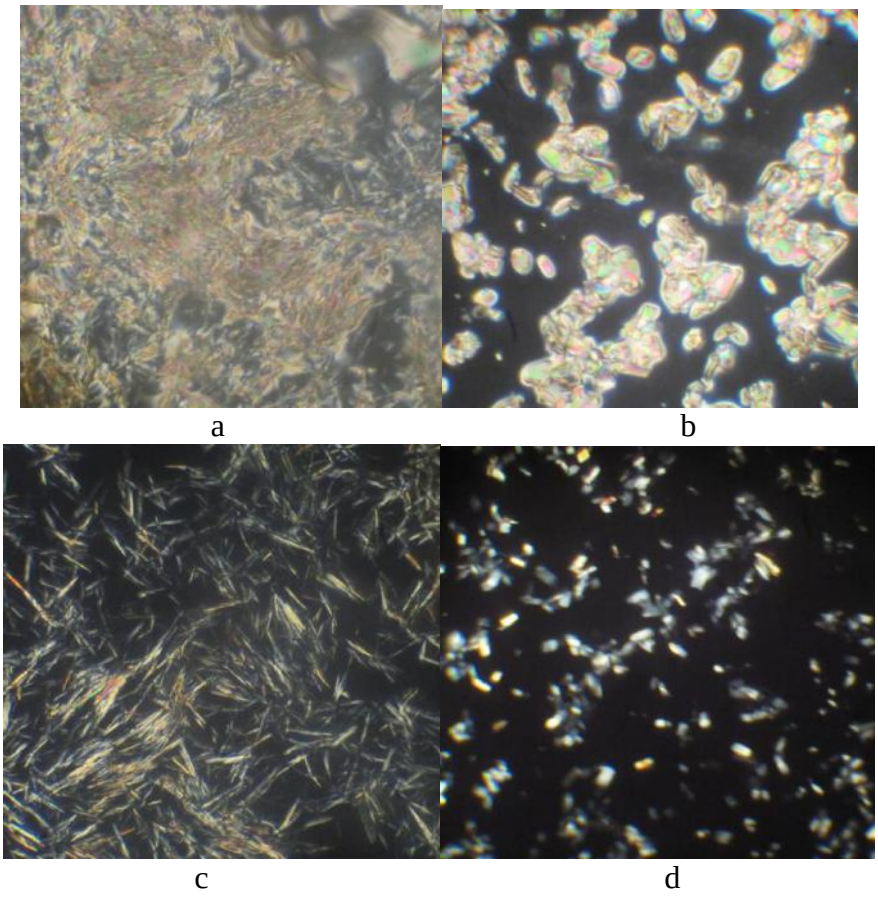

Fig. 2. Texture images under the polarizing microscope (1500 x magnification): (a) the pure LC at 34.1°C, (b) the pure LC at 34.9°C, (c) the colloid at 38.3°C, (d) the colloid at temperature 39.2°C.

As can be seen, light anisotropic areas of the pure LC texture gradually give way to dark isotropic areas in the vicinity of the phase transition (Fig. 2a and Fig. 2b). Filamentous light areas are observed for the colloid at temperature of 38.3°C (Fig.2c), which is much higher than the clearing temperature of the pure LC. It indicates that anisotropic areas near the nanorods are retained at this temperature. According to [7], LC molecules rigidly adhere to the surface of nanorods. This anchoring is maintained up to temperature of 39.0°C. Thus, the clearing point shifts to higher temperatures. It is also indicated by the temperature dependences of permittivity and electrical conductivity of the colloid (Fig. 3 and Fig. 4). It can be seen from Fig. 3 that there are different values of the longitudinal and transverse components of permittivity of the pure LC up to 35.2°C. It indicates that the substance exists in the liquid-crystalline state at indicated temperatures. We also note that the longitudinal component of the permittivity decreases while the transverse component increases in comparison with the corresponding components of the pure LC. It indicates on a decrease in the dielectric anisotropy and the order parameter which are compatible with the results of differential scanning calorimetry and polarization microscopy. After this temperature, the transverse and longitudinal components of the permittivity become equal. That is, the molecules exist in a chaotic isotropic state. An analogous situation is observed for the colloid but at temperature of 39.0°C.

Similar analysis can be carried out for temperature dependences of conductivity. Here, It can also be seen that the equalization of the transverse and longitudinal conductivity components for the pure LC occurs at temperature of 35.2°C while it takes place at temperature of 39.0°C in the colloid. That is, the results of the measurements of the temperature dependences of the conductivity of the pure LC and the colloid agree with the previous experiments. We also note that the additive of nanorods increases the conductivity of LC. Obviously, it ensues owing to the increase in the conductivity of the ionic and electronic components because of the presence of metal particles.

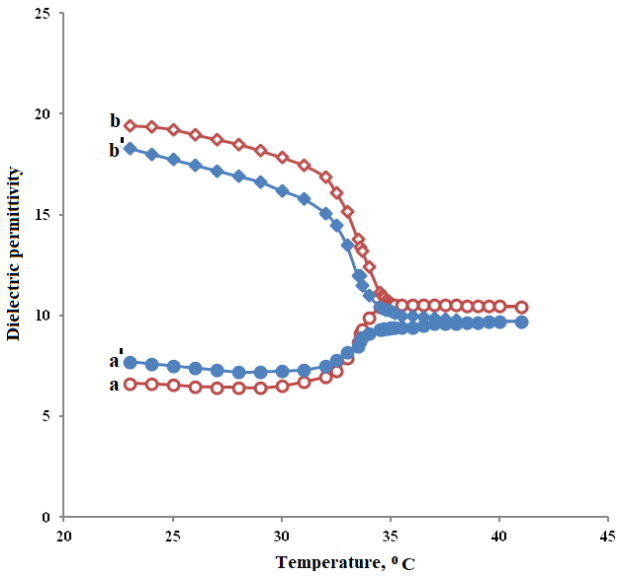

Fig 3. Temperature dependence of components of dielectric permittivity at the frequency of 2 kHz: (a) the longitudinal component of the pure LC, (a') the longitudinal component of the colloid, (b) the transverse component of the pure LC, (b') the transverse component of the colloid.

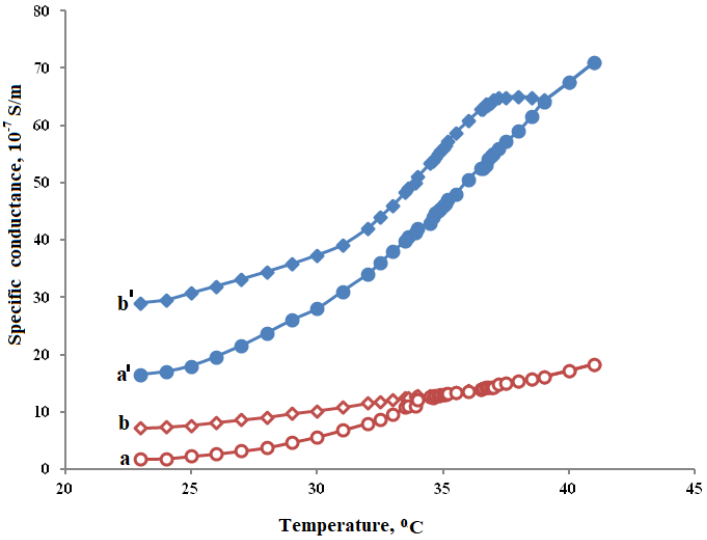

Fig. 4. Temperature dependences of specific conductance at the frequency 2 kHz: (a) the longitudinal component of the pure LC, (a') the longitudinal component of the colloid, (b) the transverse component of the pure LC, (b') the transverse component of the colloid.

Table 1 shows the numerical values of the critical temperature of transitions from the crystalline to the liquid crystalline state T_1 and the liquid crystalline to the isotropic state T_2 as well as the change in enthalpy (ΔH_1 and ΔH_2) and entropy (ΔS_1 and ΔS_2) at heating and cooling regimes calculated from Fig.1.

Table 1.

Values of the critical temperature of transitions from the crystalline to the liquid crystalline state T_1 and the liquid crystalline to the isotropic state T_2 as well as the change in enthalpy (ΔH_1 and ΔH_2) and entropy (ΔS_1 and ΔS_2) at heating and cooling regimes.

		T_1, °C	ΔH_1, J/g	ΔS_1, mJ/g ·K	T_2, °C	ΔH_2, J/g	ΔS_1, mJ/g ·K
Pure LC	heating	19.6	76.880	262.75	35.2	2.644	8.58
	cooling	14.3	0.108	0.383	33.3	-2.642	-8.62
Colloid	heating	0	0	0	39.0	2.315	7.42
	cooling	0	0	0	37.7	-1.844	-5.93

The change of thermodynamic functions is the most interesting for transition from liquid crystalline to isotropic state. As can see the change in enthalpy when adding nanorods decreases in both regimes at additive of nanorods. Moreover, it is less in the cooling regime than in the heating one.

It is known that the change of enthalpy is the energy that is absorbed or emitted as heat from a substance when it changes from one state to another and it occurs without changing of the temperature. It serves to disorganize the intermolecular bonds that hold molecules together. During curing, the reverse process (endothermic) occurs in which heat is removed from the substance. In this case, intermolecular bonds are restored, and the temperature does not change. A decrease of the change in enthalpy at both in the heating regime and the cooling one, indicates that the presence of nanorods reduces the interaction between the molecules of the LC.

The entropy of phase transition is a measure of the disorder of the substance accompanying this transition. It is sensitive to change of the arrangement of molecules and their configuration. As can be seen from Table 1, the entropy of the transition decreases with the additive of nanorods. It indicates on a decrease in the difference of the disorder degree between the liquid crystalline state and the isotropic one due to the presence of nanorods. As a result, the disorder of the liquid crystalline state of the colloid is greater than the pure LC. It is consistent with the results of dielectric measurements.

CONCLUSION

It was shown that presence of silver nanorods increase the cleaning temperature and decreases of enthalpy and entropy of transition from nematic phase to isotropic on nematic liquid crystal 5CB.

[1] *U.B. Singh, R. Dhar, R. Dabrowski, et al.* Influence of low concentration silver nanoparticles on the electrical and electro-optical parameters of nematic liquid crystals. Liq. Cryst. 40 (6) (2013) 774–782.

[2] *K.N. Singh, B. Gogoi, N.M. Singh, et al.* On the dipole–dipole correlation and dielectric anisotropy of some N (4-N-alkyloxy benzylidene) 4′-N-alkylaniline compounds doped with silver nanoparticles. Mol.Cryst.Liq. Cryst. 625(1) (2016)106–116.

[3] *B. Gogoi, K. N Singh, R. Mishra, et al.* Study of dielectric properties and the molecular dynamics using Raman spectroscopy in pure and nanoparticle doped liquid crystal compound, 6O.4. Mol.Cryst.Liq.Cryst. 646 (1) (2017) 3–13.

[4] *M. Inam, G. Singh, A. M. Biradar, D. S. Mehta.* Effect of gold nano-particles on switch-on voltage and relaxation frequency of nematic liquid crystal cell. AIP Advances, _14 (2011) 042162-1-7.

[5] *M. Mishra, R. S. Dabrowski, J. K. Vij, A. Mishra, R. Dhar.* Electrical and electro-optical parameters of 4′-octyl-4-cyanobiphenyl nematic liquid crystal dispersed with gold and silver nanoparticles. 42(11) (2015) 1580-1590.

[6] *R. Katiyar, K. Agrahari, G. Pathak, T. Vimal, G. Yadav, K. K. Pandey, A. K. Misra, A. Srivastava, R. Manohar.* Silver nanoparticles dispersed in nematic liquid crystal: an impact on dielectric and electro-optical parameters Journal of Theoretical and Applied Physics. 14 (2020) 237–243.

[7] *S.K. Prasad, K.L. Sandhya, G.G. Nair, U.S. Hiremath, C.V. Yelamaggad, S. Sampath.* Electrical conductivity and dielectric constant measurements of liquid crystal–gold nanoparticle composites. Liquid Crystals, 33(10) (2006) 1121–1125.

[8] *S. Mishra1, V. Manjuladevi, R.K. Gupta, S. Kumar.* Investigation on Physical Properties of Silver Nanorod Doped Nematic Liquid Crystal. National Conference on Physics and Chemistry of Materials AIP Conf. Proc. 2369 (2021) 020065-1-5.

Received: 11.04.2023

ISSN 1028-8546

2023, Vol. XXIX, № 2
Section: En

CONTENTS